Chapter 10
Finite Element Analysis of Planar Nonlinear Classical Beam Theories

Jonas Harsch & Simon R. Eugster

Abstract This article is based on the planar beam theories presented in Eugster and Harsch (2020) and deals with the finite element analysis of their presented beam models. A Bubnov-Galerkin method, where B-splines are chosen for both ansatz and test functions, is applied for discretizing the variational formulation of the beam theories. Five different planar beam finite element formulations are presented: The Timoshenko beam, the Euler–Bernoulli beam obtained by enforcing the cross-section's orthogonality constraint as well as the inextensible Euler–Bernoulli beam by additionally blocking the beam's extension. Furthermore, the Euler–Bernoulli beam is formulated with a minimal set of kinematical descriptors together with a constrained version that satisfies inextensibility. Whenever possible, the numerical results of the different formulations are compared with analytical and semi-analytical solutions. Additionally, numerical results reported in classical beam finite element literature are collected and reproduced.

10.1 Introduction

The finite element discretization relies on the variational formulation of the planar classical beam theories given in Eugster and Harsch (2020). With the mere choice of ansatz and test functions, the discretization of the virtual work contributions directly leads to the corresponding beam finite element formulations. Besides the time t, the virtual work contributions presented in Eugster and Harsch (2020) are parametrized by a single material coordinate s, the arc length parameter of the reference curve. With the subsequent discretization in mind, it is convenient to express the individual virtual work contributions in terms of a non arc length coordinate ξ given in the unit interval. This reparametrization is presented in Section 10.3 and yields the total

J. Harsch, S. R. Eugster
Institute for Nonlinear Mechanics, University of Stuttgart, Stuttgart, Germany
e-mail: harsch@inm.uni-stuttgart.de, eugster@inm.uni-stuttgart.de

B. E. Abali and I. Giorgio (eds.), *Developments and Novel Approaches in Nonlinear Solid Body Mechanics*, Advanced Structured Materials 130,
https://doi.org/10.1007/978-3-030-50460-1_10

virtual work of the different beam formulations given in the so-called parameter space.

The minimal formulation of the Euler–Bernoulli beam, which can be found in (Eugster and Harsch, 2020, Section 9.7.2), requires shape functions that are at least C^1-continuous. Hence, the well-known Lagrangian shape functions, being only C^0-continuous, can not be used here. Gontier and Vollmer (1995) proposed the usage of computer aided design (CAD) curve representation, such as Béziers curves, Basis splines (B-splines) or non rational B-splines (NURBS), for implementing beam finite elements. More recently, Hughes et al (2005) and Cottrell et al (2009) established the name isogeometric analysis, which unifies the fields of CAD and finite element analysis. They show the power of combining both tools for numerical analysis of partial differential equations. Led by these ideas, (Greco and Cuomo, 2013, 2014) used B-spline shape functions, which meet the above-mentioned C^1-continuity requirements, to implement a spatial Euler–Bernoulli beam. B-spline curves, which go back to the pioneering works of Schöneberg (1946) and de Boor (1972), are introduced in Section 10.4, based on the comprehensive monographs (Piegl and Tiller, 1997; Farin, 1997).

Section 10.5 shows that substituting the B-spline curves into the virtual work contributions in parameter space leads to the semi-discrete equations of motion, which are still continuous in time. If the discretized model additionally contains geometric bilateral constraints, either stemming from the constrained beam models or from enforcing boundary conditions, this leads to a set of differential algebraic equations. Although the formulations based on the Timoshenko beam model are not restricted to the above-mentioned continuity requirement, B-splines or NURBS can again be used for their discretization (Cazzani et al, 2016a,b). Another advantage over standard shape functions is, by using B-spline shape functions the global polynomial degree can be chosen arbitrarily. Thus, besides the standard h-refinement (decreasing the element length), also a p-refinement (increasing the polynomial degree) can easily be carried out. The combination of h- and p-refinement is called k-refinement (Cottrell et al, 2009; Greco and Cuomo, 2013). The discretization and all associated algorithms are generalized for any polynomial degree, which will later prove to be advantageous when studying normal modes.

Exclusive numerical examples are studied in Section 10.6. First, the presented beam formulations together with their finite element approximations are verified using analytical and semi-analytical problems from literature. Second, numerical examples of more advanced problems are treated, e.g., tracing the post-buckling equilibrium path of precurved beams. The numerical outcomes are compared with results reported in classical beam finite element literature. The article closes with conclusions and suggestions for future work.

10.2 Notation

Let $\mathbb{E}^3$ denote a three-dimensional Euclidean vector space with an orthonormal basis $\{\mathbf{e}_1, \mathbf{e}_2, \mathbf{e}_3\}$. For the discretization, all arising vector quantities from Eugster and Harsch (2020) will be expressed in this basis. For that, we collect the components of vectors $\mathbf{a} = a_1\mathbf{e}_1 + a_2\mathbf{e}_2 + a_3\mathbf{e}_3 \in \mathbb{E}^3$ in the tuple ${}_I\mathbf{a} = (a_1, a_2, a_3)^{\mathrm{T}} \in \mathbb{R}^3$. If not stated otherwise, $\mathbb{R}^f$-tuples are considered in the sense of matrix multiplication as $\mathbb{R}^{f\times 1}$-matrices, i.e., as "column vectors". Its transposed will be given by a $\mathbb{R}^{1\times f}$-matrix, i.e., a "row vector". The components of a vector rotated around $\mathbf{e}_3$ by $\frac{\pi}{2}$ is denoted by ${}_I\mathbf{a}^{\perp} = (-a_2, a_1, a_3)^{\mathrm{T}}$. Partial derivatives of vector valued functions $f\colon \mathbb{R}^f \to \mathbb{R}, \mathbf{q} \mapsto f(\mathbf{q})$, are introduced as "row vectors" $\partial f/\partial \mathbf{q} = (\partial f/\partial q^1 \cdots \partial f/\partial q^f) \in \mathbb{R}^{1\times f}$. Derivatives of functions $f = f(s,t)$ with respect to the first argument and t are denoted by a prime $f' = \partial f/\partial s$ and a dot $\dot{f} = \partial f/\partial t$, respectively. The variation of a function $f = f(s,t)$, denoted by a delta, is the derivative with respect to the parameter ε of a one-parameter family $\hat{f} = \hat{f}(s,t;\varepsilon)$ evaluated at $\varepsilon = 0$, i.e., $\delta f(s,t) = \partial \hat{f}/\partial\varepsilon(s,t;0)$. The one-parameter family satisfies $f(s,t) = \hat{f}(s,t;0)$.

10.3 Virtual Work Contributions in Parameter Space

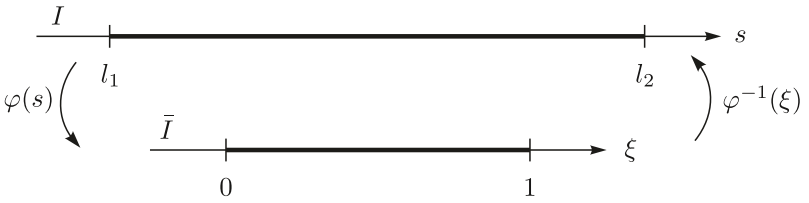

Fig. 10.1 Mapping from the material domain I to the parameter space $\bar{I}$.

As mentioned in the introduction, the parameter domain can be defined as $\bar{I} = [0,1] \subset \mathbb{R}$. Points $\xi \in \bar{I}$ belonging to the parameter domain are obtained from material points $s \in I = [l_1, l_2] \subset \mathbb{R}$ by a mapping $\varphi : I \to \bar{I}$. This new parametrization can be understood in the sense of a non arc length parametrization. We can introduce the strictly increasing function

$$\varphi\colon I \to \bar{I}\,, \quad s \mapsto \xi = \varphi(s)\,, \tag{10.1}$$

depicted in Fig. 10.1. Using the monotonicity property of (10.1), there exists an inverse function $\varphi^{-1}\colon I \to \bar{I}$, which is defined on the set $\bar{I} = \varphi(I)$, given by

$$\varphi^{-1}\colon \bar{I} \to I\,, \quad \xi \mapsto s = \varphi^{-1}(\xi)\,. \tag{10.2}$$

Let V denote some linear space, e.g., $\mathbb{R}$. With the above mappings at hand we can express an arbitrary function $f\colon I \times \mathbb{R} \to V$, e.g., the fields x, y, and θ introduced in (Eugster and Harsch, 2020), by a new function $\bar{f}\colon \bar{I} \times \mathbb{R} \to V$, defined on the parameter space $\bar{I}$.

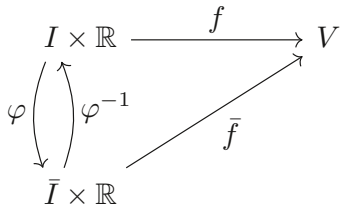

Fig. 10.2 Commutative diagram for the relations of the material coordinate s and non arc length coordinate ξ.

Since the diagram in Fig. 10.2 commutes, we find the relation

$$f(s,t) = \bar{f}(\varphi(s),t) \; . \tag{10.3}$$

Using (10.3) together with the chain rule of differential calculus, the first and second derivatives of f with respect to s are given by

$$\begin{aligned} f'(s,t) &= \frac{\partial \bar{f}}{\partial \xi}(\varphi(s),t)\frac{\mathrm{d}\varphi}{\mathrm{d}s}(s) = \bar{f}'(\varphi(s),t)\varphi'(s) \; , \\ f''(s,t) &= \frac{\partial^2 \bar{f}}{\partial \xi^2}(\varphi(s),t)\left(\frac{\mathrm{d}\varphi}{\mathrm{d}s}(s)\right)^2 + \frac{\partial \bar{f}}{\partial \xi}(\varphi(s),t)\frac{\mathrm{d}^2\varphi}{\mathrm{d}s^2}(s) \\ &= \bar{f}''(\varphi(s),t)(\varphi'(s))^2 + \bar{f}'(\varphi(s),t)\varphi''(s) \; , \end{aligned} \tag{10.4}$$

where a prime $(\cdot)'$ denotes the derivative with respect to the first argument, i.e., either s or ξ. The arc length parametrization of the reference curve $\mathbf{r}_0 = \mathbf{r}_0(s)$ is defined such that the arc length of a curve can be written as

$$l_2 - l_1 = \int_{l_1}^{l_2} \|\mathbf{r}_0'(s)\| \, \mathrm{d}s = \int_{l_1}^{l_2} \mathrm{d}s \; , \tag{10.5}$$

from which we identify $\|\mathbf{r}_0'(s)\| = 1$. This can be further manipulated using (10.4) and yields the relation for the Euclidean norm of the reference tangential vector

$$1 = \|\mathbf{r}_0'(s)\| = \|\bar{\mathbf{r}}_0'(\varphi(s))\| \, |\varphi'(s)| \; . \tag{10.6}$$

By using the property that φ is a strictly increasing function, its derivative with respect to s is positive and $\varphi'(s)$ coincides with its absolute value. Inserting these observations into (10.6), we obtain

$$\varphi'(s) = \frac{1}{\|\bar{\mathbf{r}}_0'(\varphi(s))\|} = \frac{1}{\bar{G}(\varphi(s))} \; , \tag{10.7}$$

where we have introduced $\bar{G}(\xi) = \|\bar{\mathbf{r}}_0'(\xi)\|$. The inverse function theorem yields the relation

$$(\varphi^{-1})'(\xi) = \frac{1}{\varphi'(\varphi^{-1}(\xi))} = \bar{G}(\xi) \,. \tag{10.8}$$

By repeated differentiation, the second derivative of φ is given by

$$\varphi''(s) = -\frac{\bar{\mathbf{r}}_0'(\varphi(s)) \cdot \bar{\mathbf{r}}_0''(\varphi(s))}{\bar{G}^4(\varphi(s))} \,. \tag{10.9}$$

Using the abbreviation $\mathcal{G}(\xi) = \frac{\bar{\mathbf{r}}_0'(\xi)\cdot\bar{\mathbf{r}}_0''(\xi)}{\bar{G}^2(\xi)}$, we can insert (10.7) and (10.9) into (10.4), to get

$$\begin{aligned} f'(s,t) &= \frac{\bar{f}'(\varphi(s),t)}{\bar{G}(\varphi(s))} \,, \\ f''(s,t) &= \frac{1}{\bar{G}^2(\varphi(s))} \left(\bar{f}''(\varphi(s),t) - \bar{f}'(\varphi(s),t)\mathcal{G}(\varphi(s))\right) \,. \end{aligned} \tag{10.10}$$

In the individual virtual work contributions presented by Eugster and Harsch (2020), integral expressions with respect to the material coordinate s occur. In order to formulate the total virtual work in the parameter space, all functions depending on the pair (s,t) have to be replaced with the overlined functions depending on $(\varphi(s),t)$, as shown in (10.3), together with their derivatives given in (10.10). With the help of (10.3), these integrals can be expressed by the overlined functions according to

$$\int_{l_1}^{l_2} f(s,t)\,\mathrm{d}s = \int_{l_1}^{l_2} \bar{f}(\varphi(s),t)\,\mathrm{d}s \,, \tag{10.11}$$

where derivatives with respect to s have to be computed in accordance with (10.4). Using integration by substitution, together with (10.8), the integral expression over the material domain can be computed by an integral over the parameter space given as

$$\int_{l_1=\varphi^{-1}(0)}^{l_2=\varphi^{-1}(1)} \bar{f}(\varphi(s),t)\,\mathrm{d}s = \int_0^1 \bar{f}(\xi,t)(\varphi^{-1})'(\xi)\,\mathrm{d}\xi = \int_0^1 \bar{f}(\xi,t)\bar{G}(\xi)\,\mathrm{d}\xi \,, \tag{10.12}$$

where in the first step the identity map $\xi = \varphi(\varphi^{-1}(\xi))$ was identified.

10.3.1 Timoshenko Beam

Next, we express the components of the beam's centerline $\mathbf{r}$ and the rotation angle θ by the overlined functions $\bar{\mathbf{r}}$ and $\bar{\theta}$. Moreover, we can collect their components given in the $\mathbf{e}_i$-basis in the generalized state tuple

$$\mathbf{s}(\xi,t) = (\bar{x}(\xi,t), \bar{y}(\xi,t), \bar{\theta}(\xi,t))^{\mathrm{T}} \in \mathbb{R}^3 \ . \tag{10.13}$$

By substituting the mapping φ into all arising functions, we reformulate the virtual work contributions of the inertia forces (Eugster and Harsch, 2020, (9.91)) in the following compact form

$$\delta W^{\mathrm{dyn}} = -\int_0^1 \delta\mathbf{s}^{\mathrm{T}} \bar{\boldsymbol{\Theta}} \ddot{\mathbf{s}} \bar{G} \, \mathrm{d}\xi \ , \quad \bar{\boldsymbol{\Theta}} = \begin{pmatrix} \bar{A}_{\rho_0} & 0 & 0 \\ 0 & \bar{A}_{\rho_0} & 0 \\ 0 & 0 & \bar{I}_3 \end{pmatrix} \ . \tag{10.14}$$

The virtual work contributions of the internal forces (Eugster and Harsch, 2020, (9.87)) can be computed by

$$\begin{aligned} \delta W^{\mathrm{int}} &= \int_0^1 \{\delta\mathbf{s}^{\mathrm{T}} \bar{\mathbf{t}}_1 - \delta\mathbf{s}'^{\mathrm{T}} \bar{\mathbf{t}}_2\} \, \mathrm{d}\xi \ , \\ \bar{\mathbf{t}}_1 &= (0, 0, ({}_I\bar{\mathbf{n}} \times {}_I\mathbf{e}_3)^{\mathrm{T}} \mathbf{s}')^{\mathrm{T}} \ , \quad \bar{\mathbf{t}}_2 = (\bar{n}_1, \bar{n}_2, \bar{M})^{\mathrm{T}} \ , \end{aligned} \tag{10.15}$$

where we have used $\bar{x}'\bar{n}_2 - \bar{y}'\bar{n}_1 = {}_I\mathbf{e}_3^{\mathrm{T}}(\mathbf{s}' \times {}_I\bar{\mathbf{n}}) = ({}_I\bar{\mathbf{n}} \times {}_I\mathbf{e}_3)^{\mathrm{T}}\mathbf{s}'$. Note that in both terms of the sum, $\bar{G}$ cancels with the substituted change of integration domain. In the same way the external virtual work contributions (Eugster and Harsch, 2020, (9.88)) can be expressed in the parameter domain as

$$\begin{aligned} \delta W^{\mathrm{ext}} &= \int_0^1 \delta\mathbf{s}^{\mathrm{T}} \bar{\bar{\mathbf{t}}} \bar{G} \, \mathrm{d}\xi + \sum_{i=1}^{2} \delta\mathbf{s}^{\mathrm{T}} \bar{\bar{\mathbf{t}}}_i|_{\xi=\varphi(l_i)} \ , \\ \bar{\bar{\mathbf{t}}} &= (\bar{\bar{n}}_1, \bar{\bar{n}}_2, \bar{\bar{M}})^{\mathrm{T}} \ , \quad \bar{\bar{\mathbf{t}}}_i = (\bar{\bar{n}}_1^i, \bar{\bar{n}}_2^i, \bar{\bar{M}}_i)^{\mathrm{T}} \ . \end{aligned} \tag{10.16}$$

10.3.2 Euler–Bernoulli Beam

Also for the Euler–Bernoulli beam, the overlined expressions have to be inserted. From (10.10) and the fact that the variation and the partial derivative with respect to s can be interchanged, we get

$$\mathbf{r}' = \frac{\bar{\mathbf{r}}'}{\bar{G}} \ , \quad \mathbf{r}'' = \frac{\bar{\mathbf{r}}'' - \bar{\mathbf{r}}'\mathcal{G}}{\bar{G}^2} \ , \quad \delta\mathbf{r}' = \frac{\delta\bar{\mathbf{r}}'}{\bar{G}} \ , \quad \delta\mathbf{r}'' = \frac{\delta\bar{\mathbf{r}}'' - \delta\bar{\mathbf{r}}'\mathcal{G}}{\bar{G}^2} \ . \tag{10.17}$$

The kinematical quantities defined in (Eugster and Harsch, 2020, (9.95) and (9.99)) are of the form

$$g = \frac{\|\bar{\mathbf{r}}'\|}{\bar{G}} = \frac{\bar{g}}{\bar{G}} \ , \quad \theta' = \frac{\bar{\mathbf{r}}'^{\perp} \cdot \bar{\mathbf{r}}''}{\bar{g}^2 \bar{G}} = \frac{\bar{\theta}'}{\bar{G}} \ , \tag{10.18}$$

where for the second identity we have used the property $\mathbf{a}^{\perp} \cdot \mathbf{a} = 0 \ \forall \mathbf{a} \in \mathbb{E}^3$.

Carrying out an integration by substitution, we obtain the virtual work contributions of the internal forces (Eugster and Harsch, 2020, (9.102)) given in parameter space

$$\delta W^{\mathrm{int}} = -\int_0^1 \left\{ {}_I\delta\bar{\mathbf{r}}'^{\mathrm{T}} \left(\frac{{}_I\bar{\mathbf{r}}'\bar{N}}{\bar{g}} - \frac{\bar{M}}{\bar{g}^2}\left[2\bar{\theta}'\,{}_I\bar{\mathbf{r}}' + {}_I\bar{\mathbf{r}}''^{\perp}\right] \right) + {}_I\delta\bar{\mathbf{r}}''^{\mathrm{T}}\,{}_I\bar{\mathbf{r}}'^{\perp}\frac{\bar{M}}{\bar{g}^2} \right\} \mathrm{d}\xi \,. \tag{10.19}$$

It is remarkable that all terms involving $\mathcal{G}$ cancel.

Next we can express the variation of the angle θ, its velocity and acceleration (Eugster and Harsch, 2020, (9.99) and (9.100)) by

$$\delta\theta = \frac{\bar{\mathbf{r}}'^{\perp}\cdot\delta\bar{\mathbf{r}}'}{\bar{g}^2}\,, \quad \dot{\theta} = \frac{\bar{\mathbf{r}}'^{\perp}\cdot\dot{\bar{\mathbf{r}}}'}{\bar{g}^2}\,, \quad \ddot{\theta} = \frac{\bar{\mathbf{r}}'^{\perp}\cdot\ddot{\bar{\mathbf{r}}}'}{\bar{g}^2} - \frac{2\dot{\theta}\bar{\mathbf{r}}'\cdot\dot{\bar{\mathbf{r}}}'}{\bar{g}^2}\,. \tag{10.20}$$

Inserting the above relations into (Eugster and Harsch, 2020, (9.104)), the virtual work contributions of the inertia forces in parameter space are transformed to

$$\delta W^{\mathrm{dyn}} = -\int_0^1 \left\{ \bar{I}_3 \frac{{}_I\bar{\mathbf{r}}'^{\perp\mathrm{T}}\,{}_I\delta\bar{\mathbf{r}}'}{\bar{g}^4} \left({}_I\bar{\mathbf{r}}'^{\perp\mathrm{T}}\,{}_I\ddot{\bar{\mathbf{r}}}' - 2\dot{\theta}\,{}_I\bar{\mathbf{r}}'^{\mathrm{T}}\,{}_I\dot{\bar{\mathbf{r}}}' \right) + \bar{A}_{\rho_0}\,{}_I\delta\bar{\mathbf{r}}^{\mathrm{T}}\,{}_I\ddot{\bar{\mathbf{r}}} \right\} \bar{G}\,\mathrm{d}\xi \,. \tag{10.21}$$

Finally, the virtual work contributions for the external forces (Eugster and Harsch, 2020, (9.103)) have to be expressed in parameter space. This can be done analogously to the above procedure and yields

$$\begin{aligned} \delta W^{\mathrm{ext}} = &\int_0^1 \left\{ {}_I\delta\bar{\mathbf{r}}^{\mathrm{T}}\,{}_I\bar{\bar{\mathbf{n}}} + \frac{{}_I\bar{\mathbf{r}}'^{\perp\mathrm{T}}\,{}_I\delta\bar{\mathbf{r}}'}{\bar{g}^2}\bar{\bar{M}} \right\} \bar{G}\,\mathrm{d}\xi \\ &+ \sum_{i=1}^{2} \left\{ {}_I\delta\bar{\mathbf{r}}^{\mathrm{T}}\,{}_I\bar{\bar{\mathbf{n}}}_i + \frac{{}_I\bar{\mathbf{r}}'^{\perp\mathrm{T}}\,{}_I\delta\bar{\mathbf{r}}'}{\bar{g}^2}\bar{\bar{M}}_i \right\} \Big|_{\xi=\varphi(l_i)} \,. \end{aligned} \tag{10.22}$$

10.3.3 Constraint Virtual Work Contributions

Next, also the virtual work contributions of the constraint forces are expressed in parameter space, using the same procedure as above. The planar virtual work contributions of the orthogonality constraint (Eugster and Harsch, 2020, (9.94)) are expressed in parameter space

$$\begin{aligned} \delta W^{\mathrm{int}}_{\mathrm{c},1} &= \int_0^1 \delta\bar{\sigma}_2(\mathbf{s}'^{\mathrm{T}}\,{}_I\bar{\mathbf{d}}_2)\,\mathrm{d}\xi \,, \\ \delta W^{\mathrm{int}}_{\mathrm{c},2} &= \int_0^1 \bar{\sigma}_2\{\delta\mathbf{s}'^{\mathrm{T}}\,{}_I\bar{\mathbf{d}}_2 - \delta\mathbf{s}^{\mathrm{T}}\,{}_I\mathbf{e}_3(\mathbf{s}'^{\mathrm{T}}\,{}_I\bar{\mathbf{d}}_1)\}\,\mathrm{d}\xi \,. \end{aligned} \tag{10.23}$$

Accordingly, the virtual work contributions of the inextensibility constraint (Eugster and Harsch, 2020, (9.97)) can be transformed to the integrals over the parameter space given by

$$\delta W_{\mathrm{c},1}^{\mathrm{int}} = \int_0^1 \delta\bar{\sigma}_1(\bar{g} - \bar{G})\,\mathrm{d}\xi\ , \quad \delta W_{\mathrm{c},2}^{\mathrm{int}} = \int_0^1 \bar{\sigma}_1 \frac{{}_I\delta\bar{\mathbf{r}}'^{\mathrm{T}}\,{}_I\bar{\mathbf{r}}'}{\bar{g}}\,\mathrm{d}\xi\ . \tag{10.24}$$

10.4 B-Spline Shape Functions

The excellent monograph of Piegl and Tiller (1997) gives a comprehensive introduction to the topic. They introduce B-spline shape functions and B-spline curves, together with a myriad of important properties. For this, the *knot vector* $\boldsymbol{\Xi}$ with its elements ξ_i, $i = 1, \ldots, m$ will be introduced as a non-decreasing sequence, i.e., $\xi_i \leq \xi_{i+1}$. The total number of knots is determined by the chosen polynomial degree p of the target B-spline curve and the total number n of curve sections aka elements. It can be computed as $m = n + 2p + 1$. In the subsequent treatment we restrict ourselves to

- *open* knot vectors, i.e., the multiplicity of the first and last knot is $p + 1$
- knot vectors in the unit interval $[0, 1]$
- equally spaced, so called *uniform* knot vectors, i.e., $\Delta\xi = \xi_{i+1} - \xi_i = \frac{1}{n}$ for $i = p{+}1, \ldots, n{+}p$ belonging to the interior of the knot vector

These restrictions lead to knot vectors of the form

$$\boldsymbol{\Xi} = \{\underbrace{0, \ldots, 0}_{p+1}, \underbrace{\xi_{p+2}, \ldots, \xi_{m-p-1}}_{n-1}, \underbrace{1, \ldots, 1}_{p+1}\}\ . \tag{10.25}$$

According to (Cox, 1972; de Boor, 1972; Piegl and Tiller, 1997) the ith of total $N = n{+}p$ B-spline shape functions is recursively defined as

$$\begin{aligned} N_0^i(\xi) &= \begin{cases} 1\ , & \xi \in [\xi_i, \xi_{i+1}) \\ 0\ , & \xi \notin [\xi_i, \xi_{i+1}) \end{cases}\ , \\ N_p^i(\xi) &= \frac{\xi - \xi_i}{\xi_{i+p} - \xi_i} N_{p-1}^i(\xi) + \frac{\xi_{i+p+1} - \xi}{\xi_{i+p+1} - \xi_{i+1}} N_{p-1}^{i+1}(\xi)\ , \end{aligned} \tag{10.26}$$

where in the last line possibly arising quotients of the form $\frac{0}{0}$ are defined as zero. In Fig. 10.3 all non-zero cubic shape functions for a uniform open knot vector, built of four elements, are shown.

The first derivative of a B-spline shape function can be computed from two lower order B-spline shape functions as

$$\frac{\mathrm{d}}{\mathrm{d}\xi} N_p^i(\xi) = N_{p,\xi}^i(\xi) = \frac{p}{\xi_{i+p} - \xi_i} N_{p-1}^i(\xi) - \frac{p}{\xi_{i+p+1} - \xi_{i+1}} N_{p-1}^{i+1}(\xi)\ . \tag{10.27}$$

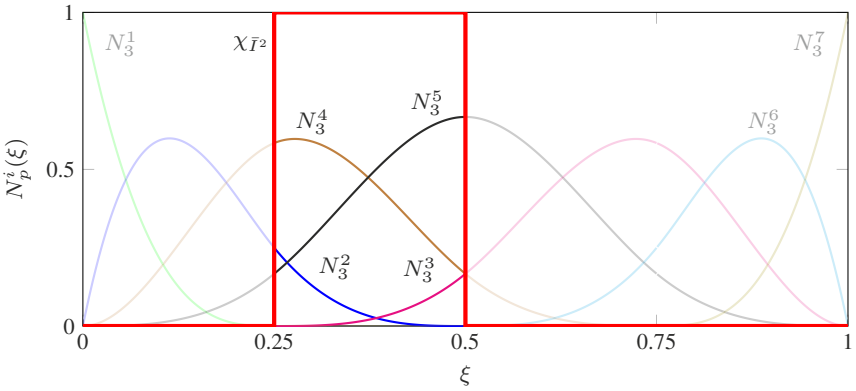

Fig. 10.3 Non-zero cubic B-spline shape functions N_3^1 to N_3^7 for a given uniform and open knot vector $\Xi = \{0, 0, 0, 0, 0.25, 0.5, 0.75, 1, 1, 1, 1\}$ which builds $n = 4$ elements. The indicator function $\chi_{\bar{I}^2}$ of the second element, defined in (10.34), picks the corresponding cubic shape functions N_3^2 to N_3^5.

Denoting the kth derivative of $N_p^i(\xi)$ by $\frac{\mathrm{d}^k}{\mathrm{d}\xi^k} N_p^i(\xi)$, repeated differentiation of (10.27) leads to the general formula

$$\begin{aligned} \frac{\mathrm{d}^k}{\mathrm{d}\xi^k} N_p^i(\xi) = & \frac{p}{\xi_{i+p} - \xi_i} \left(\frac{\mathrm{d}^{k-1}}{\mathrm{d}\xi^{k-1}} N_{p-1}^i(\xi) \right) \\ & - \frac{p}{\xi_{i+p+1} - \xi_{i+1}} \left(\frac{\mathrm{d}^{k-1}}{\mathrm{d}\xi^{k-1}} N_{p-1}^{i+1}(\xi) \right) . \end{aligned} \tag{10.28}$$

Another generalization computes the kth derivative of $N_p^i(\xi)$ by the use of the basis functions $N_{p-k}^i, \ldots, N_{p-k}^{i+k}$, namely

$$\begin{aligned} \frac{\mathrm{d}^k}{\mathrm{d}\xi^k} N_p^i(\xi) &= \frac{p!}{(p-k)!} \sum_{j=0}^{k} a_{k,j} N_{p-k}^{i+j}(\xi) , \\ a_{k,k} &= \begin{cases} 1 & k = 0 \\ \frac{a_{k-1,0}}{\xi_{i+p-k+1} - \xi_i} & k \neq 0 \end{cases} , \\ a_{k,j} &= \begin{cases} \frac{a_{k-1,0}}{\xi_{i+p-k+1} - \xi_i} & j = 0 \\ \frac{a_{k-1,j} - a_{k-1,j-1}}{\xi_{i+p+j-k+1} - \xi_{i+j}} & j = 1, \ldots, k-1 \end{cases} . \end{aligned} \tag{10.29}$$

Some knot differences in the denominator of $a_{k,j}$ given in (10.29) can be zero, the arising quotient $\frac{\bullet}{0}$ is defined as zero in these cases.[1]

[1] Piegl and Tiller (1997) present an efficient algorithm that is based on (10.29) and that computes for a given knot value ξ the value of the B-spline shape functions together with all $k = 1, \ldots, p$ non-zero derivatives. The pseudocode is given in (Piegl and Tiller, 1997, Chap. 2, p. 71, algorithm

In the following some important properties of B-spline shape functions, presented by Piegl and Tiller (1997), are listed.

P1 $N_0^i(\xi)$ is a step function, which is only non-zero in the half open interval $\bar{I}_i = [\xi_i, \xi_{i+1})$, the so called ith *knot span*.

P2 $N_p^i(\xi) = 0$ for ξ outside the knot span, which is called the *local support* property. Note that the knot vector contains $m - 1 = n + 2p$ intervals, but only n of them are non-zero. These non-zero intervals are called *element intervals* $\bar{I}^e = \bar{I}_{e+p} = [\xi_{e+p}, \xi_{e+p+1})$ and are addressed by the element number $e = i-p$. Note that we distinguish the knot span and the element interval by using a subscript and a superscript, respectively.

P3 For positive p the shape function $N_p^i(\xi)$ is a linear combination of two lower order shape functions with polynomial degree $p - 1$. This leads to a truncated triangular table which is exemplary depicted in Fig. 10.4 for B-spline shape functions up to a polynomial degree of $p = 2$. The arrows denote the influence of the current shape function on shape functions of higher polynomial degree.

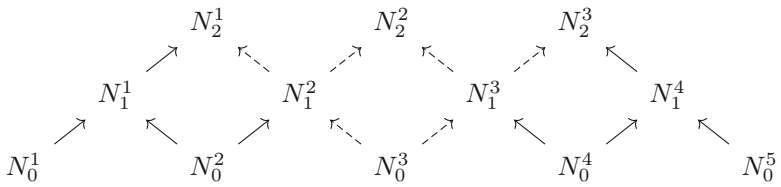

Fig. 10.4 Truncated triangular table for B-spline shape functions up to a polynomial degree of $p = 2$.

P4 For a given knot span, $\bar{I}_i = [\xi_i, \xi_{i+1})$ at most $p + 1$ shape functions N_p^i are non-zero, namely the functions $N_p^{i-p}, \ldots, N_p^i$. Using again the triangular table depicted in Fig. 10.4, we recognize that on the third knot span $\bar{I}_3 = [\xi_3, \xi_4)$, the only non-zero zeroth-degree shape function is N_0^3. Hence, the only linear and quadratic shape functions not being zero on $\bar{I}^3$ are N_1^2, N_1^3 and N_2^1, N_2^2, N_2^3, respectively. In Fig. 10.4, the dashed arrows point from or to the non-zero shape functions for the third knot span. In Fig. 10.3 the cubic shape functions for a knot vector $\boldsymbol{\Xi} = \{0, 0, 0, 0, 0.25, 0.5, 0.75, 1, 1, 1, 1\}$ are visualized. This defines a B-spline curve given by $n = 4$ elements. For the fifth knot span (second element interval) $\bar{I}_5 = \bar{I}^2 = [0.25, 0.5)$ solely four of the total seven shape functions are non-zero.

P5 All shape functions are positive, i.e., $N_p^i(\xi) \geq 0$ for all i, p, ξ. This is called the *non-negativity* property.

P6 *Partition of unity*, for all $\xi \in [\xi_i, \xi_{i+1})$ in an arbitrary knot span $\bar{I}_i = [\xi_i, \xi_{i+1})$, we have $\sum_{j=i-p}^{i} N_p^j(\xi) = 1$.

A2.3). This algorithm can be vectorized easily in order to compute all shape functions and their derivatives for a set of knot values.

P7 In the interior of a knot span, (ξ_i, ξ_{i+1}), the B-spline curve is a polynomial of degree p and thus there exist all derivatives $N_p^i(\xi)$. At a knot ξ_i, the shape function $N_p^i(\xi)$ is $p-k$ times continuously differentiable, where k is the multiplicity of the knot.[2] Hence, increasing the polynomial degree globally increases the continuity of the B-spline curve.

For uniform, open knot vectors $\boldsymbol{\Xi} \in [0, 1]$, on which we confined ourselves in the beginning of this section, a pth degree B-spline curve is defined as

$$\mathbf{c}(\xi, t) = \sum_{i=1}^{N} N_p^i(\xi)\mathbf{q}^i(t) \ , \qquad 0 \leq \xi < 1 \ , \tag{10.30}$$

where the tuple $\mathbf{q}^i$ are denoted as control points. In the sense of a Galerkin method in mechanics the N control points $\mathbf{q}^i$ are called *generalized coordinates*. The B-spline shape functions $N_p^i(\xi)$ are computed according to (10.26). A computational algorithm for evaluating (10.30) is given in (Piegl and Tiller, 1997, Chap. 3, p. 82, algorithm A3.1).

Computing the kth derivative of $\mathbf{c}(\xi, t)$, namely $\frac{\mathrm{d}^k}{\mathrm{d}\xi^k}\mathbf{c}(\xi, t)$, is done analogously to (10.30) and reads

$$\frac{\mathrm{d}^k}{\mathrm{d}\xi^k}\mathbf{c}(\xi) = \sum_{i=1}^{N} \frac{\mathrm{d}^k}{\mathrm{d}\xi^k} N_p^i(\xi)\mathbf{q}^i \ , \qquad 0 \leq \xi < 1 \ . \tag{10.31}$$

The derivatives of the shape functions have to be computed by (10.28) or (10.29). A computational algorithm for the evaluation of (10.31) is given in (Piegl and Tiller, 1997, Chap. 3, p. 93, algorithm A3.2).

10.5 Discrete Kinematics, Semidiscrete Virtual Work, and Equations of Motion

In the subsequent, treatment the continuous fields $\mathbf{s}$ and ${}_I\bar{\mathbf{r}}$ will be approximated by pth order B-spline curves. Thus the infinite-dimensional beam models are projected to finite dimensional discretized systems. Depending on the approximated field, the ith control point $\mathbf{q}^i$ is given by the tuples $\mathbf{q}^i(t) = (x^i(t), y^i(t), \theta^i(t))^{\mathrm{T}} \in \mathbb{R}^3$ or $\mathbf{q}^i(t) = (x^i(t), y^i(t))^{\mathrm{T}} \in \mathbb{R}^2$.

[2] This property is of crucial importance for the discretization of the presented Euler–Bernoulli beam. The evaluation of the internal virtual work contributions require the existence of the integral (10.19). Since this integral includes terms of second derivative, C^1-continuity of the chosen interpolation polynomial is required. For polynomial degrees $p \geq 2$ this continuity requirement is unconditionally fulfilled.

10.5.1 Timoshenko Beam

The generalized coordinates are collected in the tuple of generalized coordinates

$$\mathbf{q} = (x^1, \dots, x^N, y^1, \dots, y^N, \theta^1, \dots, \theta^N)^{\mathrm{T}} \in \mathbb{R}^{3N} \ . \tag{10.32}$$

Thus, the generalized state tuple (10.13) can be approximated by the pth order B-spline curve

$$\mathbf{s}(\xi, t) \approx \mathbf{c}\big(\xi, \mathbf{q}(t)\big) = \sum_{i=1}^{N} N_p^i(\xi)\mathbf{q}^i(t) \ . \tag{10.33}$$

In a Galerkin method, it is convenient to evaluate the kinematic quantities in an element-wise setting. As mentioned in P4, for a given element e and its corresponding element interval $\bar{I}^e = [\xi_{e+p}, \xi_{e+p+1})$, several B-spline shape functions are non-zero. Thus, we have to partly consider multiple shape functions. In order to extract the correct parts of the shape functions and to not consider the same parts multiple times, the indicator function

$$\chi_{\bar{I}^e} \colon \mathbb{R} \to \mathbb{R} \ , \quad \chi_{\bar{I}^e}(\xi) = \begin{cases} 1 \ , & \xi \in \bar{I}^e \\ 0 \ , & \xi \notin \bar{I}^e \end{cases} \tag{10.34}$$

is introduced. See Fig. 10.3 for a graphical visualization. With the above definition at hand, (10.33) can be written as

$$\mathbf{c}\big(\xi, \mathbf{q}(t)\big) = \sum_{e=1}^{n} \sum_{i=1}^{N} \chi_{\bar{I}^e}(\xi) N_p^i(\xi)\mathbf{q}^i(t) \ . \tag{10.35}$$

As written in P4, for a given knot span $\bar{I}_i = \bar{I}^{i-p}$, only $p+1$ B-spline shape functions are non-zero, namely $N_p^{i-p}, \dots, N_p^i$. Thus instead of summing over all N shape functions, we can equivalently write

$$\mathbf{c}\big(\xi, \mathbf{q}(t)\big) = \sum_{e=1}^{n} \sum_{i=e}^{e+p} \chi_{\bar{I}^e}(\xi) N_p^i(\xi)\mathbf{q}^i(t) \ , \tag{10.36}$$

where we have shifted the shape function index using the relation between knot span and element number given by $i = e + p$. The inner sum can be computed by the matrix tuple product

$$\mathbf{c}\big(\xi, \mathbf{q}(t)\big) = \sum_{e=1}^{n} \chi_{\bar{I}^e}(\xi)\mathbf{c}^e \ , \quad \mathbf{c}^e = \mathbf{N}_p^e(\xi)\mathbf{q}^e(t) \ . \tag{10.37}$$

It is composed of the element matrix of the B-spline shape functions $\mathbf{N}_p^e \in \mathbb{R}^{3\times 3(p+1)}$ and the element generalized coordinate tuple $\mathbf{q}^e \in \mathbb{R}^{3(p+1)}$, each of which is defined as

$$\mathbf{N}_p^e = \begin{pmatrix} N_p^e & N_p^{e+1} & \dots & N_p^{e+p} & 0 & 0 & \dots & 0 & 0 & 0 & \dots & 0 \\ 0 & 0 & \dots & 0 & N_p^e & N_p^{e+1} & \dots & N_p^{e+p} & 0 & 0 & \dots & 0 \\ 0 & 0 & \dots & 0 & 0 & 0 & \dots & 0 & N_p^e & N_p^{e+1} & \dots & N_p^{e+p} \end{pmatrix} ,$$
$$\mathbf{q}^e = (x^e, x^{e+1}, \dots, x^{e+p}, y^e, y^{e+1}, \dots, y^{e+p}, \theta^e, \theta^{e+1}, \dots, \theta^{e+p})^{\mathrm{T}} . \quad (10.38)$$

Using the Boolean allocation matrix $\mathbf{C}^e \in \mathbb{R}^{3(p+1)\times 3N}$, the relationship of the element coordinates $\mathbf{q}^e$ and the global nodal coordinates $\mathbf{q}$ is given by

$$\mathbf{q}^e = \mathbf{C}^e \mathbf{q} . \quad (10.39)$$

Let the generalized velocities $\dot{\mathbf{q}}$, generalized accelerations $\ddot{\mathbf{q}}$ and the first variation of the generalized coordinates $\delta\mathbf{q}$ be of the same form as (10.32). By transferring the relation between the element coordinates and the global ones from (10.39), we are able to approximate the first and second spatial derivatives, the acceleration, as well as the variation of the generalized state tuple by

$$\begin{aligned} \mathbf{s}'(\xi,t) &\approx \mathbf{c}'\big(\xi, \mathbf{q}(t)\big) = \sum_{e=1}^{n} \chi_{\bar{I}^e}(\xi) \mathbf{N}_p^{e\prime}(\xi) \mathbf{C}^e \mathbf{q}(t) , \\ \mathbf{s}''(\xi,t) &\approx \mathbf{c}''\big(\xi, \mathbf{q}(t)\big) = \sum_{e=1}^{n} \chi_{\bar{I}^e}(\xi) \mathbf{N}_p^{e\prime\prime}(\xi) \mathbf{C}^e \mathbf{q}(t) , \\ \ddot{\mathbf{s}}(\xi,t) &\approx \ddot{\mathbf{c}}\big(\xi, \mathbf{q}(t)\big) = \sum_{e=1}^{n} \chi_{\bar{I}^e}(\xi) \mathbf{N}_p^{e}(\xi) \mathbf{C}^e \ddot{\mathbf{q}}(t) , \\ \delta\mathbf{s}(\xi,t) &\approx \delta\mathbf{c}\big(\xi, \mathbf{q}(t)\big) = \sum_{e=1}^{n} \chi_{\bar{I}^e}(\xi) \mathbf{N}_p^{e}(\xi) \mathbf{C}^e \delta\mathbf{q}(t) . \end{aligned} \quad (10.40)$$

Furthermore, we can substitute the approximations for the variation and acceleration of the generalized state tuple given in (10.40), into the planar virtual work of the inertia contributions in parameter space (10.14). Recapitulating that the characteristic function is non-zero only if $\xi \in \bar{I}^e$, either one of the characteristic functions vanishes if the two arising sums have not the same index, thus the product of two sums reduces to a single one and we get

$$\delta W^{\mathrm{dyn}} \approx -\int_0^1 \sum_{e=1}^{n} \chi_{\bar{I}^e} \delta\mathbf{q}^{\mathrm{T}} \mathbf{C}^{e\mathrm{T}} \mathbf{N}_p^{e\,\mathrm{T}} \bar{\boldsymbol{\Theta}} \mathbf{N}_p^e \mathbf{C}^e \ddot{\mathbf{q}} \bar{G} \, \mathrm{d}\xi . \quad (10.41)$$

For a given element e, the characteristic function extracts the element interval $\bar{I}^e = [\xi_e, \xi_{e+1})$ from the parameter space $\bar{I} = [0,1]$. Thus, the integral over the whole parameter space $\bar{I}$ reduces to an integral over the element interval $\bar{I}^e$. Accordingly, we obtain after minor rearrangements

$$\delta W^{\mathrm{dyn}} \approx -\delta\mathbf{q}^{\mathrm{T}} \sum_{e=1}^{n} \mathbf{C}^{e\mathrm{T}} \int_{\xi_e}^{\xi_{e+1}} \mathbf{N}_p^{e\mathrm{T}} \bar{\boldsymbol{\Theta}} \mathbf{N}_p^e \bar{G} \, \mathrm{d}\xi \; \mathbf{C}^e \ddot{\mathbf{q}} = -\delta\mathbf{q}^{\mathrm{T}} \mathbf{M} \ddot{\mathbf{q}} . \quad (10.42)$$

The global and elemental mass matrices $\mathbf{M}$ and $\mathbf{M}^e$, respectively, are obtained as

$$\mathbf{M} = \sum_{e=1}^{n} \mathbf{C}^{e\mathrm{T}} \mathbf{M}^e \mathbf{C}^e \ , \quad \mathbf{M}^e = \int_{\xi_e}^{\xi_{e+1}} \mathbf{N}_p^{e\mathrm{T}} \bar{\mathbf{\Theta}} \mathbf{N}_p^e \bar{G} \, \mathrm{d}\xi \ . \tag{10.43}$$

Further we used that $\delta\mathbf{q}$ and $\ddot{\mathbf{q}}$ are independent of ξ and therefore can be pulled out the integral.

Accordingly, the internal virtual work contributions in the parameter space, given in (10.15), can be approximated by

$$\begin{aligned} \delta W^{\mathrm{int}} &\approx \delta\mathbf{q}^{\mathrm{T}} \mathbf{f}^{\mathrm{int}} \ , \quad \mathbf{f}^{\mathrm{int}} = \sum_{e=1}^{n} \mathbf{C}^{e\mathrm{T}} \mathbf{f}^{\mathrm{int},e} \ , \\ \mathbf{f}^{\mathrm{int},e} &= \int_{\xi_e}^{\xi_{e+1}} \left\{ \mathbf{N}_p^{e\mathrm{T}} \bar{\mathbf{t}}_1 - \mathbf{N}_p^{e\prime\mathrm{T}} \bar{\mathbf{t}}_2 \right\} \mathrm{d}\xi \ , \end{aligned} \tag{10.44}$$

where we have introduced the global internal forces $\mathbf{f}^{\mathrm{int}}$ and their elemental contributions $\mathbf{f}^{\mathrm{int},e}$. With some straightforward computations, the internal stiffness matrix $\mathbf{K} = \frac{\partial \mathbf{f}^{\mathrm{int}}}{\partial \mathbf{q}}$ can be computed as

$$\begin{aligned} \mathbf{K} &= \sum_{e=1}^{n} \mathbf{C}^{e\mathrm{T}} \mathbf{K}^e \mathbf{C}^e \ , \quad \mathbf{K}^e = \int_{\xi_e}^{\xi_{e+1}} \left\{ \mathbf{N}_p^{e\mathrm{T}} \frac{\partial \bar{\mathbf{t}}_1}{\partial \mathbf{q}^e} - \mathbf{N}_p^{e\prime\mathrm{T}} \frac{\partial \bar{\mathbf{t}}_2}{\partial \mathbf{q}^e} \right\} \mathrm{d}\xi \ , \\ \frac{\partial \bar{\mathbf{t}}_1}{\partial \mathbf{q}^e} &= \left(\frac{\partial 0}{\partial \mathbf{q}^e}, \frac{\partial 0}{\partial \mathbf{q}^e}, ({}_I\bar{\mathbf{n}} \times {}_I\mathbf{e}_3)^{\mathrm{T}} \mathbf{N}_p^{e\prime} + ({}_I\mathbf{e}_3 \times \mathbf{c}^{e\prime})^{\mathrm{T}} \frac{\partial {}_I\bar{\mathbf{n}}}{\partial \mathbf{q}^e} \right)^{\mathrm{T}} \ , \\ \frac{\partial \bar{\mathbf{t}}_2}{\partial \mathbf{q}^e} &= \left(\frac{\partial \bar{n}_1}{\partial \mathbf{q}^e}, \frac{\partial \bar{n}_2}{\partial \mathbf{q}^e}, \frac{\partial \bar{M}}{\partial \mathbf{q}^e} \right)^{\mathrm{T}} \ . \end{aligned} \tag{10.45}$$

Using the same procedure as for the inertia and internal virtual work contributions, we obtain the discretized form of the external virtual work contributions in parameter space (10.16) given by

$$\begin{aligned} \delta W^{\mathrm{ext}} &\approx \delta\mathbf{q}^{\mathrm{T}} (\mathbf{f}^{\mathrm{ext}} + \sum_{i=1}^{2} \mathbf{f}_i^{\mathrm{ext}}) \ , \quad \mathbf{f}^{\mathrm{ext}} = \sum_{e=1}^{n} \mathbf{C}^{e\mathrm{T}} \mathbf{f}^{\mathrm{ext},e} \ , \\ \mathbf{f}^{\mathrm{ext},e} &= \int_{\xi_e}^{\xi_{e+1}} \mathbf{N}_p^{e\mathrm{T}} \bar{\mathbf{t}} \bar{G} \, \mathrm{d}\xi \ , \quad \mathbf{f}_i^{\mathrm{ext}} = \sum_{e=1}^{n} \mathbf{C}^{e\mathrm{T}} \chi_{\bar{I}^e} \mathbf{N}_p^{e\mathrm{T}} \bar{\mathbf{t}}_i |_{\xi=\varphi(l_i)} \ . \end{aligned} \tag{10.46}$$

10.5.2 Euler–Bernoulli Beam

For the discretization of the Euler–Bernoulli beam, only the first $2N$ generalized coordinates of (10.32) are collected in a new generalized coordinate tuple

$$\mathbf{q} = (x^1, \dots, x^N, y^1, \dots, y^N)^{\mathrm{T}} \in \mathbb{R}^{2N} \ . \tag{10.47}$$

Similarly to (10.37), the components of the position vector given in the $\mathbf{e}_i$-basis can be approximated by

$${}_I\bar{\mathbf{r}}(\xi, t) \approx \mathbf{c}\big(\xi, \mathbf{q}(t)\big) = \sum_{e=1}^{n} \chi_{\bar{I}^e}(\xi)\mathbf{c}^e \ , \quad \mathbf{c}^e = \mathbf{N}_p^e(\xi)\mathbf{q}^e(t) \ . \tag{10.48}$$

The element matrix of the B-spline shape functions $\mathbf{N}_p^e \in \mathbb{R}^{2\times 2(p+1)}$ and the element generalized coordinate tuple $\mathbf{q}^e \in \mathbb{R}^{2(p+1)}$ are defined as

$$\begin{aligned} \mathbf{N}_p^e &= \begin{pmatrix} N_p^e & N_p^{e+1} & \dots & N_p^{e+p} & 0 & 0 & \dots & 0 \\ 0 & 0 & \dots & 0 & N_p^e & N_p^{e+1} & \dots & N_p^{e+p} \end{pmatrix} \ , \\ \mathbf{q}^e &= (x^e, x^{e+1}, \dots, x^{e+p}, y^e, y^{e+1}, \dots, y^{e+p})^{\mathrm{T}} \ . \end{aligned} \tag{10.49}$$

Using a new Boolean allocation matrix $\mathbf{C}^e \in \mathbb{R}^{2(p+1)\times 2N}$, the relationship of the element coordinates $\mathbf{q}^e$ and global nodal coordinates $\mathbf{q}$ is again given by $\mathbf{q}^e = \mathbf{C}^e\mathbf{q}$. Inserting the approximations for all required kinematic quantities into (10.21), we get the approximated virtual work contributions of the inertia forces

$$\begin{aligned} \delta W^{\mathrm{dyn}} &\approx -\delta\mathbf{q}^{\mathrm{T}}\mathbf{M}\ddot{\mathbf{q}} + \delta\mathbf{q}^{\mathrm{T}}\mathbf{h} \ , \ \mathbf{M} = \sum_{e=1}^{n} \mathbf{C}^{e\mathrm{T}}\mathbf{M}^e\mathbf{C}^e \ , \ \mathbf{h} = \sum_{e=1}^{n} \mathbf{C}^{e\mathrm{T}}\mathbf{h}^e \ , \\ \mathbf{M}^e &= \int_{\xi_e}^{\xi_{e+1}} \left(\bar{A}_{\rho_0}\mathbf{N}_p^{e\mathrm{T}}\mathbf{N}_p^e + \frac{\bar{I}_3}{\bar{g}^4}(\mathbf{N}_p^{e\prime\mathrm{T}}\mathbf{c}^{e\prime\perp})(\mathbf{c}^{e\prime\perp\mathrm{T}}\mathbf{N}_p^{e\prime}) \right) \bar{G}\,\mathrm{d}\xi \ , \\ \mathbf{h}^e &= \int_{\xi_e}^{\xi_{e+1}} \frac{2\dot{\theta}\bar{I}_3}{\bar{g}^4}(\mathbf{N}_p^{e\prime\mathrm{T}}\mathbf{c}^{e\prime\perp})(\mathbf{c}^{e\prime\mathrm{T}}\dot{\mathbf{c}}^{e\prime})\bar{G}\,\mathrm{d}\xi \ . \end{aligned} \tag{10.50}$$

Note, that in addition to the mass matrix $\mathbf{M}$, a gyroscopic force $\mathbf{h}$ and its elemental counterpart $\mathbf{h}^e$ appears. Both $\mathbf{h}$ and $\mathbf{h}^e$ are quadratic in $\dot{\mathbf{q}}$ and $\dot{\mathbf{q}}^e$, respectively.

Accordingly, the internal virtual work contributions (10.19) can be approximated by

$$\begin{aligned} \delta W^{\mathrm{int}} &\approx \delta\mathbf{q}^{\mathrm{T}}\mathbf{f}^{\mathrm{int}} \ , \quad \mathbf{f}^{\mathrm{int}} = \sum_{e=1}^{n} \mathbf{C}^{e\mathrm{T}}\mathbf{f}^{\mathrm{int},e} \ , \\ \mathbf{f}^{\mathrm{int},e} &= -\int_{\xi_e}^{\xi_{e+1}} \left\{ \mathbf{N}_p^{e\prime\mathrm{T}} \left(\frac{\mathbf{c}^{e\prime}\bar{N}}{\bar{g}} - \frac{\bar{M}}{\bar{g}^2}\left[2\bar{\theta}'\mathbf{c}^{e\prime} + \mathbf{c}^{e\prime\prime\perp}\right] \right) \right. \\ &\qquad \left. + \mathbf{N}_p^{e\prime\prime\mathrm{T}}\mathbf{c}^{e\prime\perp}\frac{\bar{M}}{\bar{g}^2} \right\} \mathrm{d}\xi \ . \end{aligned} \tag{10.51}$$

Using basic rules of calculus, the stiffness matrix can be derived as

$$
\begin{aligned}
\mathbf{K} &= \frac{\partial \mathbf{f}^{\mathrm{int}}}{\partial \mathbf{q}} = \sum_{e=1}^{n} \mathbf{C}^{e\mathrm{T}} \mathbf{K}^{e} \mathbf{C}^{e} \ , \\
\mathbf{K}^{e} &= \int_{\xi_e}^{\xi_{e+1}} \left\{ \mathbf{N}_p^{e\prime\prime\mathrm{T}} \left(k_2 \frac{\partial \mathbf{c}^{e\prime\perp}}{\partial \mathbf{q}^{e}} + \mathbf{c}^{e\prime\perp} \frac{\partial k_2}{\partial \mathbf{q}^{e}} \right) \right. \\
&\quad \left. + \mathbf{N}_p^{e\prime\mathrm{T}} \left[\frac{\partial \mathbf{k}_1}{\partial \mathbf{q}^{e}} - \left(\mathbf{k}_3 + \mathbf{c}^{e\prime\prime\perp} \right) \frac{\partial k_2}{\partial \mathbf{q}^{e}} - k_2 \left(\frac{\partial \mathbf{k}_3}{\partial \mathbf{q}^{e}} + \frac{\partial \mathbf{c}^{e\prime\prime\perp}}{\partial \mathbf{q}^{e}} \right) \right] \right\} \mathrm{d}\xi \ .
\end{aligned}
\tag{10.52}
$$

The introduced auxiliary functions and their partial derivatives with respect to the generalized coordinates are given by

$$
\begin{aligned}
\mathbf{k}_1 &= \frac{\mathbf{c}^{e\prime} \bar{N}}{\bar{g}} \ , \quad \frac{\partial \mathbf{k}_1}{\partial \mathbf{q}^{e}} = -\frac{\mathbf{k}_1}{\bar{g}} \frac{\partial \bar{g}}{\partial \mathbf{q}^{e}} + \frac{1}{\bar{g}} \left(\bar{N} \mathbf{N}_p^{e\prime} + \mathbf{c}^{e\prime} \frac{\partial \bar{N}}{\partial \mathbf{q}^{e}} \right) \ , \\
k_2 &= \frac{\bar{M}}{\bar{g}^2} \ , \quad \frac{\partial k_2}{\partial \mathbf{q}^{e}} = -2 \frac{k_2}{\bar{g}} \frac{\partial \bar{g}}{\partial \mathbf{q}^{e}} + \frac{1}{\bar{g}^2} \frac{\partial \bar{M}}{\partial \mathbf{q}^{e}} \ , \\
\mathbf{k}_3 &= 2 \bar{\theta}' \mathbf{c}^{e\prime} \ , \quad \frac{\partial \mathbf{k}_3}{\partial \mathbf{q}^{e}} = 2 \left(\mathbf{c}^{e\prime} \frac{\partial \bar{\theta}'}{\partial \mathbf{q}^{e}} + \bar{\theta}' \mathbf{N}_p^{e\prime} \right) \ , \\
\frac{\partial \bar{g}}{\partial \mathbf{q}^{e}} &= \frac{\mathbf{c}^{e\prime}}{\bar{g}} \mathbf{N}_p^{e\prime} \ , \quad \frac{\partial \bar{\theta}'}{\partial \mathbf{q}^{e}} = \frac{1}{\bar{g}^2} \left(\mathbf{c}^{e\prime\perp\mathrm{T}} \mathbf{N}_p^{e\prime\prime} - \mathbf{c}^{e\prime\prime\mathrm{T}} \frac{\partial \mathbf{c}^{e\prime\perp}}{\partial \mathbf{q}^{e}} \right) - 2 \frac{\bar{\theta}'}{\bar{g}} \frac{\partial \bar{g}}{\partial \mathbf{q}^{e}} \ .
\end{aligned}
\tag{10.53}
$$

Finally, the external virtual work contributions in parameter space given in (10.22) can be discretized by

$$
\begin{aligned}
\delta W^{\mathrm{ext}} &\approx \delta \mathbf{q}^{\mathrm{T}} (\mathbf{f}^{\mathrm{ext}} + \sum_{i=1}^{2} \mathbf{f}_i^{\mathrm{ext}}) \ , \quad \mathbf{f}^{\mathrm{ext}} = \sum_{e=1}^{n} \mathbf{C}^{e\mathrm{T}} \mathbf{f}^{\mathrm{ext},e} \ , \\
\mathbf{f}^{\mathrm{ext},e} &= \int_{\xi_e}^{\xi_{e+1}} \left\{ \mathbf{N}_p^{e\mathrm{T}} \bar{\mathbf{n}} + \mathbf{N}_p^{e\prime\mathrm{T}} \mathbf{c}^{e\prime\perp} \frac{\bar{M}}{\bar{g}^2} \right\} \bar{G} \, \mathrm{d}\xi \ , \\
\mathbf{f}_i^{\mathrm{ext}} &= \sum_{e=1}^{n} \mathbf{C}^{e\mathrm{T}} \chi_{\bar{I}^e} \left\{ \mathbf{N}_p^{e\mathrm{T}} \bar{\mathbf{n}}_i + \mathbf{N}_p^{e\prime\mathrm{T}} \mathbf{c}^{e\prime\perp} \frac{\bar{M}_i}{\bar{g}^2} \right\} \Big|_{\xi=\varphi(l_i)} \ .
\end{aligned}
\tag{10.54}
$$

10.5.3 Constraint Forces

In addition to the discretization of the position and rotation fields, the contributions of the constraint forces (10.23) and (10.24) have to be discretized. This is done by approximating the Lagrange multiplier fields $\bar{\sigma}_1$ and $\bar{\sigma}_2$ using B-spline curves in accordance with (10.37), i.e., the same element distribution for the Lagrange multiplier fields and the kinematic quantities is chosen. Two new sets of generalized coordinates can be introduced

$$
\mathbf{q}_{\sigma_1} = (\bar{\sigma}_1^1, \ldots, \bar{\sigma}_1^N)^{\mathrm{T}} \in \mathbb{R}^N \ , \quad \mathbf{q}_{\sigma_2} = (\bar{\sigma}_2^1, \ldots, \bar{\sigma}_2^N)^{\mathrm{T}} \in \mathbb{R}^N \ . \tag{10.55}
$$

Thus for $k = 1, 2$, both Lagrange multipliers can be approximated by the B-spline curve of polynomial degree p_{σ_k} given as

$$\begin{aligned} \bar{\sigma}_k(\xi, t) \approx c_k\big(\xi, \mathbf{q}_{\sigma_k}(t)\big) = \sum_{e=1}^{n} \chi_{\bar{I}^e}(\xi) c_k^e \,, \\ c_k^e = \mathbf{N}_{p_{\sigma_k}}^e(\xi) \mathbf{q}_{\sigma_k}^e(t) \,, \quad \mathbf{q}_{\sigma_k}^e = \mathbf{C}_{\sigma_k}^e \mathbf{q}_{\sigma_k} \,. \end{aligned} \tag{10.56}$$

The element tuple of the B-spline shape functions $\mathbf{N}_{p_{\sigma_k}}^e \in \mathbb{R}^{1 \times p_{\sigma_k}+1}$ and the element generalized coordinate tuple $\mathbf{q}_{\sigma_k}^e \in \mathbb{R}^{p_{\sigma_k}+1}$ are defined as

$$\mathbf{N}_{p_{\sigma_k}}^e = (N_{p_{\sigma_k}}^e, N_{p_{\sigma_k}}^{e+1}, \ldots, N_{p_{\sigma_k}}^{e+p_{\sigma_k}}) \,, \quad \mathbf{q}_{\sigma_k}^e = (\bar{\sigma}_k^e, \bar{\sigma}_k^{e+1}, \ldots, \bar{\sigma}_k^{e+p_{\sigma_k}})^{\mathrm{T}} \,. \tag{10.57}$$

The question arises, which polynomial degree p_{σ_k} for the approximation of the Lagrange multipliers is compatible with the polynomial degree p of the approximated kinematic quantities. Without further investigations, we chose the polynomial degree $p_{\sigma_k} = p - 1$ in the subsequent treatment. Numerical experiments have shown, that such a polynomial degree leads to good convergence and accuracy of the constraint beam models. By substituting the approximation of the Lagrange multiplier fields given in (10.56) into the constraint virtual work contributions (10.23), the approximated version reads

$$\begin{aligned} \delta W_{\mathrm{c},1}^{\mathrm{int}} &= \delta \mathbf{q}_{\sigma_2}^{\mathrm{T}} \mathbf{g}_{\sigma 2}, \; \mathbf{g}_{\sigma_2} = \sum_{e=1}^{n} \mathbf{C}_{\sigma_2}^{e\mathrm{T}} \mathbf{g}_{\sigma_2}^e, \; \mathbf{g}_{\sigma_2}^e = \int_{\xi_e}^{\xi_{e+1}} \mathbf{N}_{p_{\sigma_2}}^{e\mathrm{T}} ({\mathbf{c}^{e\prime\mathrm{T}}}_I \bar{\mathbf{d}}_2) \, \mathrm{d}\xi \,, \\ \delta W_{\mathrm{c},2}^{\mathrm{int}} &= \delta \mathbf{q}^{\mathrm{T}} \mathbf{f}_{\mathrm{c}}^{\mathrm{int}} = \delta \mathbf{q}^{\mathrm{T}} \mathbf{W}_{\sigma_2} \mathbf{q}_{\sigma_2} \,, \quad \mathbf{W}_{\sigma_2} = \sum_{e=1}^{n} \mathbf{C}^{e\mathrm{T}} \mathbf{W}_{\sigma_2}^e \mathbf{C}_{\sigma_2}^e \,, \\ \mathbf{W}_{\sigma_2}^e &= \int_{\xi_e}^{\xi_{e+1}} \big\{ \mathbf{N}_p^{e\prime\mathrm{T}}{}_I \bar{\mathbf{d}}_2 - \mathbf{N}_p^{e\mathrm{T}}{}_I \mathbf{e}_3 ({\mathbf{c}^{e\prime\mathrm{T}}}_I \bar{\mathbf{d}}_1) \big\} \mathbf{N}_{p_{\sigma_2}}^e \, \mathrm{d}\xi \,. \end{aligned} \tag{10.58}$$

From the above we can identify the generalized force directions by the partial derivative of the discretized constraint function, i.e., $\mathbf{W}_{\sigma_2}^{\mathrm{T}} = \partial \mathbf{g}_{\sigma_2} / \partial \mathbf{q}$ and $\mathbf{W}_{\sigma_2}^{e\mathrm{T}} = \partial \mathbf{g}_{\sigma_2}^e / \partial \mathbf{q}^e$.

For the inextensibility condition introduced in (10.24), the same steps as above can be performed which yields

$$\begin{aligned} \delta W_{\mathrm{c},1}^{\mathrm{int}} &= \delta \mathbf{q}_{\sigma_1}^{\mathrm{T}} \mathbf{g}_{\sigma_1} \,, \; \mathbf{g}_{\sigma_1} = \sum_{e=1}^{n} \mathbf{C}_{\sigma_1}^{e\mathrm{T}} \mathbf{g}_{\sigma_1}^e \,, \; \mathbf{g}_{\sigma_1}^e = \int_{\xi_e}^{\xi_{e+1}} \mathbf{N}_{p_{\sigma_1}}^{e\mathrm{T}} (\bar{g} - \bar{G}) \, \mathrm{d}\xi \,, \\ \delta W_{\mathrm{c},2}^{\mathrm{int}} &= \delta \mathbf{q}^{\mathrm{T}} \mathbf{f}_{\mathrm{c}}^{\mathrm{int}} = \delta \mathbf{q}^{\mathrm{T}} \mathbf{W}_{\sigma_1} \mathbf{q}_{\sigma_1} \,, \quad \mathbf{W}_{\sigma_1} = \sum_{e=1}^{n} \mathbf{C}^{e\mathrm{T}} \mathbf{W}_{\sigma_1}^e \mathbf{C}_{\sigma_1}^e \,, \\ \mathbf{W}_{\sigma_1}^e &= \int_{\xi_e}^{\xi_{e+1}} \mathbf{N}_p^{e\prime\mathrm{T}} \frac{\mathbf{c}^{e\prime}}{\bar{g}} \mathbf{N}_{p_{\sigma_1}}^e \, \mathrm{d}\xi \,. \end{aligned} \tag{10.59}$$

Again, the generalized force directions can be identified with the partial derivative of the discretized constraint functions with respect to the generalized coordinates, i.e. $\mathbf{W}_{\sigma_1}^{\mathrm{T}} = \partial \mathbf{g}_{\sigma_1} / \partial \mathbf{q}$ and $\mathbf{W}_{\sigma_1}^{e\mathrm{T}} = \partial \mathbf{g}_{\sigma_1}^{e} / \partial \mathbf{q}^{e}$.

10.5.4 Equations of Motion and Bilateral Constraints

The principle of virtual work, stated in (Eugster and Harsch, 2020, (9.56)), can be formulated in a discrete way by inserting the discrete virtual work contributions presented in the previous section. The total virtual work has to vanish for all admissible variations $\delta\mathbf{q}$ of the generalized coordinates and for any instant of time t, i.e.

$$\delta W = \delta W^{\mathrm{dyn}} + \delta W^{\mathrm{int}} + \delta W^{\mathrm{ext}} = 0 \,, \qquad \forall \delta\mathbf{q},\ \forall t \,. \tag{10.60}$$

Substituting the generalized forces introduced in Section 10.5.1 and demanding it to hold for arbitrary variations $\delta\mathbf{q}$ for all time t, we get

$$\begin{aligned} -\delta\mathbf{q}^{\mathrm{T}} \left(\mathbf{M}(\mathbf{q})\ddot{\mathbf{q}} - \mathbf{f}^{\mathrm{int}}(\mathbf{q}) - \mathbf{f}^{\mathrm{ext}}(\mathbf{q}, \dot{\mathbf{q}}, t) \right) = 0 \,, \quad \forall \delta\mathbf{q}, \forall t \\ \Rightarrow \mathbf{M}(\mathbf{q})\ddot{\mathbf{q}} - \mathbf{f}^{\mathrm{int}}(\mathbf{q}) - \mathbf{f}^{\mathrm{ext}}(\mathbf{q}, \dot{\mathbf{q}}, t) = 0 \,, \end{aligned} \tag{10.61}$$

which are the semidiscrete equations of motion of the planar Timoshenko beam, which hold for all time instants t.

Similarly, the semidiscrete equations of motion of the planar Euler–Bernoulli beam are obtained by substituting the discrete counterparts of the virtual work contributions given in Section 10.5.2 into the principle of virtual work, which leads to

$$\mathbf{M}(\mathbf{q})\ddot{\mathbf{q}} - \mathbf{h}(\mathbf{q}, \dot{\mathbf{q}}) - \mathbf{f}^{\mathrm{int}}(\mathbf{q}) - \mathbf{f}^{\mathrm{ext}}(\mathbf{q}, \dot{\mathbf{q}}, t) = 0 \,. \tag{10.62}$$

Furthermore, the virtual work contributions of the constraint forces can be added to both discrete virtual work principles given above. The constrained Euler–Bernoulli beam is obtained by incorporating the angle constraint (10.58) in the total virtual work of the Timoshenko beam. Further the inextensibility condition (10.59) can be added, which yields the constrained inextensible Euler–Bernoulli beam formulation. The discretized minimal formulated Euler–Bernoulli beam can be made inextensible by the very same constraint condition. Next, depending on the desired constrained beam formulation, the generalized vector of constraints $\mathbf{g}_{\sigma_1}$, respectively $\mathbf{g}_{\sigma_2}$ are named $\mathbf{g}_{\sigma}$ when only one constraint condition is applied. Or both constraints $\mathbf{g}_{\sigma_1}$ and $\mathbf{g}_{\sigma_2}$ are stacked in the tuple $\mathbf{g}_{\sigma}$. In an analogous fashion, the corresponding generalized coordinates tuple $\mathbf{q}_{\sigma}$ is built. Similarly, one of the generalized force directions $\mathbf{W}_{\sigma_1}$ and $\mathbf{W}_{\sigma_2}$ is named $\mathbf{W}_{\sigma}$ when only a single set of constraints is required, or we can assemble $\mathbf{W}_{\sigma_1}$ and $\mathbf{W}_{\sigma_2}$ in a matrix $\mathbf{W}_{\sigma}$, when both sets of constraints are imposed. Thus, independent of the chosen set of constraints, the equations of motion for the constrained beam models are given by

$$\begin{aligned} \mathbf{M}(\mathbf{q})\ddot{\mathbf{q}} - \mathbf{f}^{\mathrm{int}}(\mathbf{q}) - \mathbf{f}^{\mathrm{ext}}(\mathbf{q},\dot{\mathbf{q}},t) - \mathbf{W}_\sigma(\mathbf{q})\mathbf{q}_\sigma &= 0 \\ \mathbf{g}_\sigma(\mathbf{q}) &= 0\ . \end{aligned} \tag{10.63}$$

It is convenient to introduce another set of perfect bilateral constraints $\mathbf{g}(\mathbf{q},t) \in \mathbb{R}^f$ which enforce the prescribed kinematic boundary conditions. Their associated generalized force directions are $\mathbf{W}^{\mathrm{T}} = \partial\mathbf{g}/\partial\mathbf{q}$ with $\mathbf{W} \in \mathbb{R}^{3N\times f}$ or $\mathbf{W} \in \mathbb{R}^{2N\times f}$ for the Timoshenko and Euler–Bernoulli beam model, respectively. The corresponding tuple of Lagrange multipliers is $\boldsymbol{\lambda} \in \mathbb{R}^f$. The discrete equations of motion are extended with the constraint force contributions $\mathbf{W}(\mathbf{q},t)\boldsymbol{\lambda}$, together with the additional constraint conditions $\mathbf{g}(\mathbf{q},t)$ and read

$$\begin{aligned} \mathbf{M}(\mathbf{q})\ddot{\mathbf{q}} - \mathbf{f}^{\mathrm{int}}(\mathbf{q}) - \mathbf{f}^{\mathrm{ext}}(\mathbf{q},\dot{\mathbf{q}},t) - \mathbf{W}_\sigma(\mathbf{q})\mathbf{q}_\sigma - \mathbf{W}(\mathbf{q},t)\boldsymbol{\lambda} &= 0 \\ \mathbf{g}_\sigma(\mathbf{q}) &= 0 \\ \mathbf{g}(\mathbf{q},t) &= 0\ . \end{aligned} \tag{10.64}$$

They have to be solved for the unknowns $\{\mathbf{q},\mathbf{q}_\sigma,\boldsymbol{\lambda}\}$. In case of the Euler–Bernoulli beam model the gyroscopic force vector $\mathbf{h}$ has to subtracted from the left-hand side of the first equality in (10.63) and (10.64).

Both (10.63) and (10.64) are sets of differential algebraic equations (DAE) of index 3. A general introduction to DAE solvers is given in Hairer and Wanner (2002), including the standard methods like *Shake*, *Rattle* and *backward differentiation formula (BDF)*. In structural dynamics the generalized-α method is a well-established solver, not only because of its simple implementation, but also because of its ability to eliminate the contribution of non-physical high-frequency modes. Variants of the generalized α-method for constraint mechanical systems are introduced in (Lunk and Simeon, 2006; Arnold and Brüls, 2007; Jay and Negrut, 2009). In order to include unilateral constraints (Leine and van de Wouw, 2007), a more recent variant of the generalized-α method is proposed by Brüls et al (2014, 2018).

The static equilibrium problem is obtained by omitting the inertia terms and allowing the external forces and the bilateral constraints to depend only on the generalized coordinates $\mathbf{q}$. This leads to the static residual equation

$$\mathbf{R}(\mathbf{q},\mathbf{q}_\sigma,\boldsymbol{\lambda}) = \left(\mathbf{f}^{\mathrm{int}}(\mathbf{q}) + \mathbf{f}^{\mathrm{ext}}(\mathbf{q}) + \mathbf{W}_\sigma(\mathbf{q})\mathbf{q}_\sigma + \mathbf{W}(\mathbf{q})\boldsymbol{\lambda},\ \mathbf{g}_\sigma(\mathbf{q}),\ \mathbf{g}(\mathbf{q})\right)^{\mathrm{T}}\ . \tag{10.65}$$

Application of a truncated Taylor-series expansion of (10.65) around a given point $\{\mathbf{q}_0,\mathbf{q}_{\sigma_0},\boldsymbol{\lambda}_0\}$ yields a Newton–Raphson type iteration scheme, which solves for the unknowns $\{\mathbf{q},\mathbf{q}_\sigma,\boldsymbol{\lambda}\}$.

Finally, the arising element integrals over the domain $\bar{I}^e = [\xi_e,\xi_{e+1}]$ in the individual parts of the equations of motion have to be computed. This is done by using a numerical integration scheme. The basic idea of numerical quadrature is the approximation of the integral $\int_a^b f(\xi)\ \mathrm{d}\xi$ in a given interval $I = [a,b]$ by evaluating the function f at some discrete values $\xi_i \in I$ and multiplication with the so-called integration weights w_i. Since numerical quadrature rules are well known in literature, the reader is referred to basic textbooks about numerical analysis, e.g., (Stoer et al, 2002, Chap. 3) and (Quarteroni et al, 2000, Chap. 9-10). The

numerical examples, presented in the subsequent section are computed using the Gauss-Legendre quadrature rule, whereby the number of quadrature points within one element are chosen such that they equal the polynomial degree p of the B-spline curves.

10.6 Numerical Examples

The subsequent section deals with the performed numerical examples. At first, we present some static benchmark problems that show the differences of the finite element implementations of all beam models and their numerical accuracy with respect to analytical solutions. Afterwards more advanced problems are investigated, including buckling problems, which are compared to numerical and semi-analytical solutions found in literature. Finally, the natural frequencies of the presented Euler–Bernoulli beam formulation will be compared to the analytically derived ones.

All presented beam models are implemented in an in-house object oriented multibody dynamics code written in Python. The data found in literature is digitalized using the amazing Webplotdigitizer tool developed by Rohatgi (2019).

10.6.1 Pure Bending of a Cantilever Beam

In the first example a straight beam of length $L = 2\pi$, axial stiffness $E_1 = 5$, shear stiffness $E_2 = 1$, and bending stiffness $F_3 = 2$ is subjected to a concentrated end couple $\overline{M}_2 = 2\pi F_3/L$. The exact solution for this problem is given by a closed circle of radius $r = 1$. This static boundary condition (pure bending) leads to a homogenous flexural deformation. There should be neither extensional nor shear effects, thus we expect all beam models leading to the very same solution. By regarding the computed configurations depicted in Fig. 10.5, this expectation has come true.

Next, the convergence behavior of all five presented beam formulations were investigated, namely the Timoshenko beam (T_1), the Euler–Bernoulli beam obtained by adding the corresponding constraint (T_2), the inextensible Euler–Bernoulli beam given by additionally adding the inextensibility condition (T_3), the minimal formulation of the Euler–Bernoulli beam (E_1) and the inextensible Euler–Bernoulli beam obtained by adding the corresponding constraint condition (E_2). All beam formulations presented in the previous sections were computed with different number of elements $n \in \{8, 16, 32, 64, 128\}$ (h-refinement) and polynomial degrees $p \in \{2, 3, 5\}$ (p-refinement). The Lagrange multiplier fields for the constrained beam models were discretized with B-splines of polynomial degree $p_{\sigma_k} = p - 1$. Further information regarding the different refinement strategies, including combinations of h-and p-refinement, the so-called k-refinement, can be found in (Cottrell et al, 2009; Greco and Cuomo, 2013). For each refinement level, 50 iterations of a force controlled Newton–Raphson method were performed using a convergence

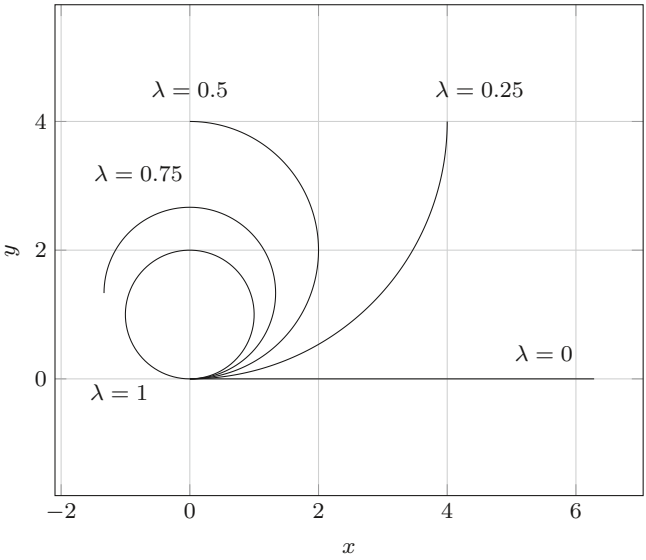

Fig. 10.5 Same configurations for all presented beam models with load increments $\lambda \in \{0, 0.25, 0.5, 0.75, 1\}$.

tolerance of 10^{-12} with respect to the maximum absolute error of the static residual (10.65). Let e be the Euclidean error of the point of applied couple with respect to the analytical solution, given by the origin. In Fig. 10.6, the normalized error e/L is depicted. By increasing the polynomial degree or the number of used finite elements, the error decreases. Two more remarkable observations can be made. The minimal formulations of the Timoshenko and Euler–Bernoulli beam led to the same errors as their constrained counterparts. This is due to the absence of axial and shear deformations in this problem. Thus, the constraints have no influence on the convergence behavior. For the finest discretization ($n = 128$ and $p = 5$), all beam models converge to an error of $\mathcal{O}(10^{-12})$, which coincides with the given tolerance of the underlying Newton–Raphson scheme.

Henceforth, we restrict the presentation to the three kinematically different beam models. For computational efficiency the models with the smallest number of degrees of freedom are chosen. These are the Timoshenko beam model (T_1), the minimal formulation of the Euler–Bernoulli beam (E_1) and its inextensible version (E_2).

10.6.2 Cantilever Beam Subjected to Constant End Load

Let us consider an initially straight beam of length $L = 2\pi$, axial stiffness $E_1 = 5$, shear stiffness $E_2 = 1$, and bending stiffness $F_3 = 2$ which is subjected to a constant end load in negative vertical direction. For the inextensible Euler–Bernoulli beam,

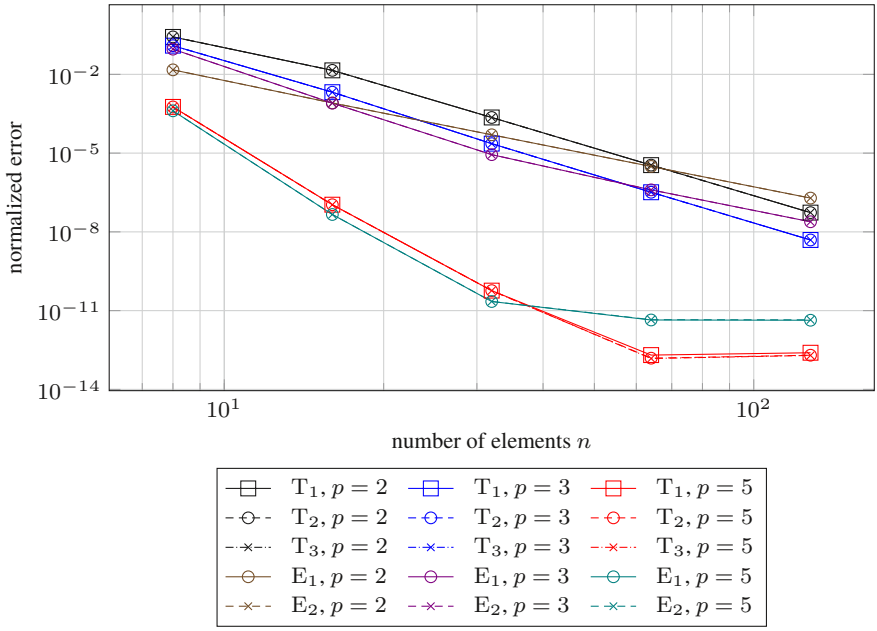

Fig. 10.6 Normalized Euclidean error of the point of applied couple with respect to the analytical solution, given by the origin, for all different beam models using different levels of refinement.

this kind of problem is solved analytically using the first and second elliptic integrals, defined as

$$F(\theta,k)=\int_0^\theta (1-k^2\sin^2\tilde{\theta})^{-\frac{1}{2}}\,\mathrm{d}\tilde{\theta}\;,\quad E(\theta,k)=\int_0^\theta (1-k^2\sin^2\tilde{\theta})^{\frac{1}{2}}\,\mathrm{d}\tilde{\theta}\;. \tag{10.66}$$

Byrd and Friedman (1954) give a general introduction to elliptic integrals. Let

$${}_I\mathbf{F}=-P\,{}_I\mathbf{e}_2\;,\quad P=\left(\frac{\alpha}{L}\right)^2 F_3\;, \tag{10.67}$$

be an external point force at the beam's end $s=L$ depending on a force parameter α^2. Bisshopp and Drucker (1945) derived the solution for the horizontal and vertical deflection of the cantilever beam in terms of the elliptic integrals given in (10.66), i.e.,

$$\begin{aligned} x(L)&=\frac{L\sqrt{2}}{\alpha}\sqrt{\sin\phi_0}\;,\quad \sin\phi_0=2k^2-1\;,\\ y(L)&=L\left(1-\frac{2}{\alpha}\left[E(\pi/2,k)-E(\theta_1,k)\right]\right)\;,\quad \sin\theta_1=\frac{\sqrt{2}}{2k}\;. \end{aligned} \tag{10.68}$$

The deflections solely depend on the parameter k. Bisshopp and Drucker (1945) showed that the inextensibility condition leads to

$$\alpha = F(\pi/2, k) - F(\theta_1, k) \; . \tag{10.69}$$

By using a root-finding method, e.g., a bisection method, for a given load value α^2, the corresponding k value can be obtained. This completely determines the displacement of the beam tip of the inextensible Euler–Bernoulli beam.

For the discretization of the used finite element models, $n = 20$ quadratic B-spline elements ($p = 2$, $p_{\sigma_1} = 1$) were used. The numerical solution was obtained by application of a load controlled Newton–Raphson method with 10 load steps and a convergence tolerance of 10^{-8} with respect to the maximum absolute error of the static residual (10.65).

In Fig. 10.7, the configurations for the different beam models are compared with the solution found by using elliptic integrals. For the inextensible Euler–Bernoulli beam model all configurations are in excellent accordance with the elliptic integral solution. The Euler–Bernoulli beam model leads to the same curvature but due to its extensibility the end points do not coincide with the elliptic integral solution. For the Timoshenko beam additionally shear deformation is allowed. Thus also the curvatures do not coincide with those of the inextensible Euler–Bernoulli beam solutions.

In Fig. 10.8, the normalized horizontal and vertical displacements given by $\delta = -y(L)/L$ and $\Delta = x(L)/L$ are depicted for given load parameters α^2. It can be observed that the inextensible Euler–Bernoulli beam model can reproduce the results obtained by using elliptic integrals. The Timoshenko and Euler–Bernoulli beam models lead to slightly different results, due to presence of extensional and shear deformations.

10.6.3 Cantilever Beam Subject to Follower End Load

In this example the large deflection of a cantilever beam of length $L = 1$, axial stiffness $E_1 = EA$ ($E = 2100$, $A = 20 \cdot 10^{-4}$), shear stiffness $E_2 = GA$ ($G = E/(2 + 2\nu)$, $\nu = 0.3$), flexural stiffness $F_3 = EI$ ($I = 1,667 \cdot 10^{-8}$) under non-conservative transverse force is investigated. This problem was examined by (Argyris and Symeonidis, 1981; Simo and Vu-Quoc, 1986). The beam is clamped on the left-hand side and on the right-hand side a transverse follower force $\mathbf{F}$ with $||\mathbf{F}|| = \lambda 3 \cdot 10^{-3}$ is applied. The force is applied perpendicular to the beam tip. The angle between the free end and the applied force thus always remains $\pi/2$.

For the discretization of the used finite element models, $n = 20$ quadratic B-spline elements ($p = 2$, $p_{\sigma_1} = 1$) were used. The numerical solution was obtained by application of a load controlled Newton–Raphson method with 100 load steps and a convergence tolerance of 10^{-8} with respect to the maximum absolute error of the static residual (10.65).

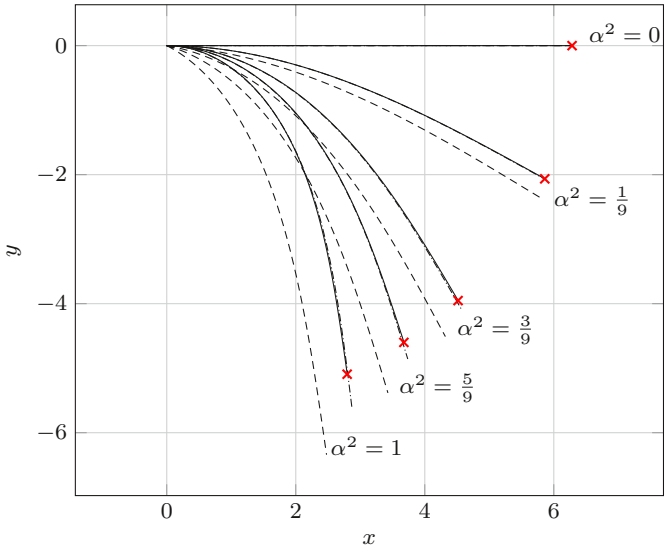

Fig. 10.7 Configurations for different load parameters $\alpha^2 \in \{0, \frac{1}{9}, \frac{3}{9}, \frac{5}{9}, 1\}$. The Timoshenko beam is depicted by dashed lines, the Euler–Bernoulli beam by dashdotted lines and the inextensible Euler–Bernoulli beam model by solid lines. The elliptic integral solutions given in Bisshopp and Drucker (1945) are indicated by red crosses.

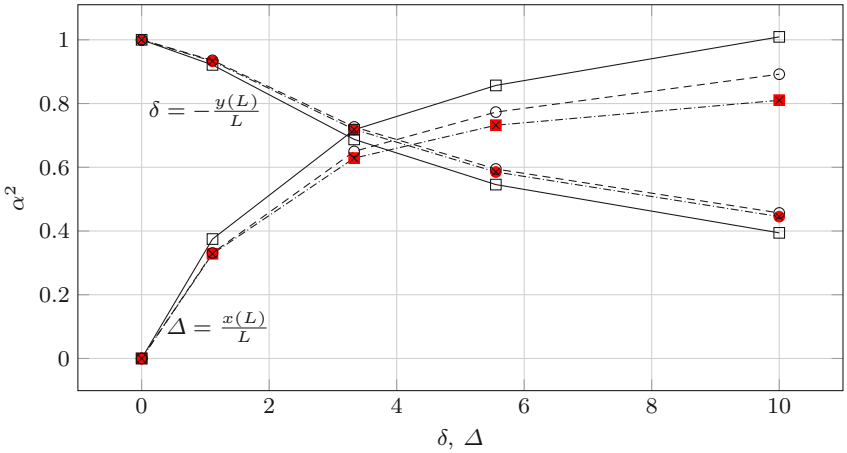

Fig. 10.8 Force displacement curves for the cantilever beam. The analytical solutions using elliptic integrals are depicted by red bullets and squares for the δ and Δ values, respectively. The finite element solutions of the Timoshenko beam are depicted by solid lines, the Euler–Bernoulli beam by dashed lines and the inextensible Euler–Bernoulli beam model by dashdotted lines.

For small load increments, the configurations of the different beam formulations, depicted in Fig 10.9, can't be distinguished. For increasing load increments, the configurations obtained by the Timoshenko beam model differ from the ones obtained by the two Euler–Bernoulli beams. The effect of the inextensibility can not be recognized.

In Fig. 10.10 the load deflection curve is compared with the results obtained by Argyris and Symeonidis (1981). There is a good overall accordance. For the loads between $\lambda = 0.1$ and $\lambda = 0.2$ the horizontal displacement curves are separated for all beam models. In contrast to Argyris and Symeonidis (1981), larger load increments were computed, in order to see slightly differences of the Timoshenko and Euler–Bernoulli beam models. Again the inextensible Euler–Bernoulli beam can not be distinguished from the extensible one.

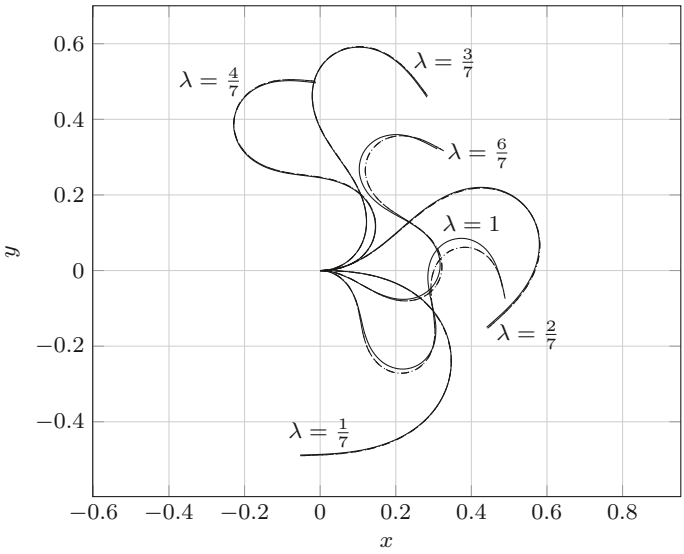

Fig. 10.9 Deformed configurations of the different beam models under a non-conservative follower force with load parameters $\lambda \in \left\{\frac{1}{7}, \frac{2}{7}, \frac{3}{7}, \frac{4}{7}, \frac{6}{7}, 1\right\}$. The Timoshenko beam model is depicted by solid lines, the Euler–Bernoulli beam by dashed lines and the inextensible Euler–Bernoulli beam model by dashdotted lines.

10.6.4 Clamped-Hinged Circular Arch Subject to Point Load

In this example, we investigated the buckling and post-buckling behavior of a circular arch of radius $R = 100$ clamped on the right end and hinged on the left, see Fig. 10.11. This problem is also discussed in (Dadeppo and Schmidt, 1975; Simo and Vu-Quoc, 1986), both of which are using an inextensible Euler–Bernoulli beam model, either

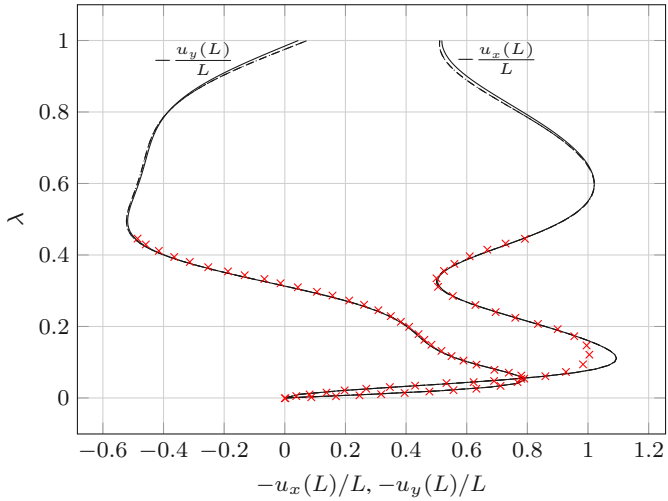

Fig. 10.10 Load deflection curves for the horizontal displacement $u_x = x(L) - L$ and vertical displacement $u_y = -y(L)$ of the point of applied load. The Timoshenko beam model is depicted by solid lines, the Euler–Bernoulli beam with dashed lines and the inextensible Euler–Bernoulli beam model by dashdotted lines. The results found in Argyris and Symeonidis (1981) are depicted by red crosses.

by direct formulation or by utilizing a penalty approach, for their investigations. The inner angle of the arc is $2\alpha = 205°$. The arch is represented by two beams of axial stiffness $E_1 = 50$, shear stiffness $E_2 = 10$ and flexural stiffness $F_3 = 1000$. The beams are connected by the use of bilateral constraints that guarantee the same position and angle at the connection point. Both beams are of undeformed length $L_1 = L_2 = 100\frac{180°}{\alpha}$. A constant external force ${}_I\mathbf{F} = -\lambda_I \mathbf{e}_2$ is applied at the crown of the circle.

B-spline shape functions are not able to represent perfect archs. In order to obtain a pre-curved reference configuration an optimization technique was developed. Let $\{\mathbf{p}_i\}$, $i = 1, \dots k$ be a given set of points $\mathbf{p}_i \in \mathbb{R}^2$, which describe the target curve of the reference configuration. Next a set of evaluation points ξ_i is collected in a knot vector $\boldsymbol{\Xi} \in \mathbb{R}^f$. There are several possibilities found in literature (Piegl and Tiller, 1997, Chap. 9.2, p. 364). The most simple method is choosing equally spaced knots in the interval $[0, 1]$. Next a pth order B-spline curve divided into n elements, which depends on the chosen polynomial degree p and the $N = n + p$ generalized coordinates $\{\mathbf{q}_j\}$, $j = 1, \dots, N$, can be introduced. The generalized coordinates $\mathbf{q}_j \in \mathbb{R}^2$ are collected in a tuple $\mathbf{q} \in \mathbb{R}^N$. Solving the optimization problem

$$K = \sum_{i=1}^{k} \frac{1}{2} \|\mathbf{c}(\xi_i, \mathbf{q}) - \mathbf{p}_i\|^2 \to \min \,, \tag{10.70}$$

leads to an optimal fit of the B-spline curve $\mathbf{c}$, defined in (10.48), to the points $\mathbf{p}_i$ in a least squares sense. The necessary condition for solving the minimization problem (10.70) reads $\partial K/\partial \mathbf{q} = 0$. Inserting the definition of the B-spline curve given in (10.48) and after carrying out minor rearrangements, we obtain the linear system of equations

$$\begin{aligned} \mathbf{A}\mathbf{q} = \mathbf{b}\,, \quad \mathbf{A} &= \sum_{i=1}^{k}\sum_{e=1}^{n} \chi_{\bar{I}^e}(\xi_i)\mathbf{C}^{e\mathrm{T}}\mathbf{N}_p^{e\mathrm{T}}(\xi_i)\mathbf{N}_p^{e}(\xi_i)\mathbf{C}^{e}\,, \\ \mathbf{b} &= \sum_{i=1}^{k}\sum_{e=1}^{n} \chi_{\bar{I}^e}(\xi_i)\mathbf{C}^{e\mathrm{T}}\mathbf{N}_p^{e\mathrm{T}}(\xi_i)\mathbf{p}_i\,. \end{aligned} \tag{10.71}$$

This can be solved for the unknown generalized coordinates $\mathbf{q}$ of the reference configuration. As a requirement for $\mathbf{A}$ to be well-conditioned, every knot span must contain at least one ξ_i, see (Piegl and Tiller, 1997, Chap. 9.4.1, p. 412) and (de Boor, 1978, Chap. 14.4, p. 223).

In order to obtain the B-spline curve representing the angle, i.e., ${}_I\mathbf{e}_3^{\mathrm{T}}\mathbf{c}(\xi,\mathbf{q})$, with $\mathbf{c}$ from (10.37), in a second step an analogous minimization problem has to be solved. The angle of the target curve can be computed by $\bar{\theta}_i = \arctan(\bar{y}'(\xi_i,\mathbf{q})/\bar{x}'(\xi_i,\mathbf{q}))$. The values for $\bar{x}'$ and $\bar{y}'$ are obtained as the first and second component of the B-spline curve's derivative $\mathbf{c}'$ given in (10.70). The new minimization problem reads

$$K^* = \sum_{i=1}^{k} \frac{1}{2}\|{}_I\mathbf{e}_3^{\mathrm{T}}\mathbf{c}(\xi_i,\mathbf{q}) - \bar{\theta}_i\|^2 \to \min\,. \tag{10.72}$$

In the discretization, presented in the previous section, we restricted ourselves to open knot vectors, thus we had to ensure that the first and last point $\mathbf{p}_1$ and $\mathbf{p}_k$, respectively exactly match with the generalized coordinates $\mathbf{q}_1$ and $\mathbf{q}_N$. Analogously, the angles have to coincide with angles of the target curve. This was obtained by additionally imposing constraints onto (10.70) and (10.72). These constraints are met by extending the system with a Lagrange multiplier method, see (Piegl and Tiller, 1997, Chap. 9.4.2).

In order to obtain post-buckling solutions, i.e., configurations after exceeding a critical force value, a numerical path following algorithm was used instead of the classical Newton–Raphson method. The most simple methods are the so-called linear arc length methods. The first solution method was published by Riks (1979), followed by others, e.g., Crisfield (1981). A general introduction to the topic of path-following and arc length methods can be found in Crisfield (1991). In order to use these solvers, together with bilateral constraints, some modifications are required. The basic ideas are sketched below. First, in contrast to a load incremented solution technique, the load parameter λ becomes an additional degree of freedom. Thus, one additional equation has to be found, in order to close the static equilibrium problem. This is done by introducing a new scalar function $f(\mathbf{q},\lambda)$, limiting the incremental displacements. As proposed by Crisfield (1991) the simple function $f(\mathbf{q},\lambda) = (\mathbf{q}-\mathbf{q}_0)^{\mathrm{T}}(\mathbf{q}-\mathbf{q}_0) - \Delta s^2$, with $\mathbf{q}_0$ being the last converged set of

generalized coordinates lying on the equilibrium path and Δs some given incremental length leads to good convergence. Next the extended residual equation

$$\mathbf{R}(\mathbf{q}, \mathbf{q}_\sigma, \boldsymbol{\lambda}, \lambda) = \begin{pmatrix} \mathbf{f}^{\mathrm{int}}(\mathbf{q}) + \lambda \mathbf{f}^{\mathrm{ext}}(\mathbf{q}) + \mathbf{W}_\sigma(\mathbf{q})\mathbf{q}_\sigma + \mathbf{W}(\mathbf{q})\boldsymbol{\lambda} \\ \mathbf{g}_\sigma(\mathbf{q}) \\ \mathbf{g}(\mathbf{q}) \\ f(\mathbf{q}, \lambda) \end{pmatrix} \tag{10.73}$$

has to be linearized around the last converged set of generalized coordinates, i.e., around $\{\mathbf{q}_0, \mathbf{q}_{\sigma 0}, \boldsymbol{\lambda}_0, \lambda_0\}$. This directly yields the modified Newton–Raphson iteration scheme. The choice of a predictor solution, in the beginning of each increment, has to be made with special care, see Crisfield (1991) for an extensive discussion.

In the present example each of the two beam finite element models was build by using $n = 20$ quadratic B-spline elements ($p = 2$, $p_{\sigma_1} = 1$). The numerical solution was obtained by using the linear arc length solver presented above with an incremental length $\Delta s = 0.08$, together with a convergence tolerance of 10^{-6} with respect to the maximum absolute error of the extended residual (10.73).

In Fig. 10.11, five pre- and post-buckling configurations of the different beam models are depicted, where the post-buckling configurations are forming a loop. In contrast to Dadeppo and Schmidt (1975), the post-buckling configurations are also computed. It can be seen that for increasing load parameters the three beam models lead to slightly different configurations. The Timoshenko beam, as the softest beam, yields the largest deflection for $\lambda = 1$. The Euler–Bernoulli beam and its inextensible version are stiffer and thus the deformation for the total external force are smaller compared to the Timoshenko beam.

The load deflection curves for the horizontal and vertical deflection of the circles apex are depicted in Fig. 10.12. For the inextensible Euler–Bernoulli beam, the results found in (Dadeppo and Schmidt, 1975) and (Simo and Vu-Quoc, 1986) are in good accordance. The buckling load for the different beam models are $\lambda_{\mathrm{b}} = 0.8297$ (Timoshenko), $\lambda_{\mathrm{b}} = 0.8805$ (Euler-Bernoulli), $\lambda_{\mathrm{b}} = 0.9102$ (inextensible Euler-Bernoulli). For the inextensible Euler–Bernoulli beam the buckling load is in good agreement with the values reported by (Simo and Vu-Quoc, 1986, $\lambda_{\mathrm{b}} = 0.90528$) and (Dadeppo and Schmidt, 1975, $\lambda_{\mathrm{b}} = 0.897$). In (Simo and Vu-Quoc, 1986) a second limit point is identified with the load value $\lambda_{\mathrm{b}} = -0.0771$, which only slightly differs from the value $\lambda_{\mathrm{b}} = -0.0807$ obtained by the presented inextensible Euler–Bernoulli beam model.

10.6.5 Buckling of a Hinged Right-Angle Frame under Follower Point Load

In this example the buckling of a both sided hinged right-angle frame of height and length 120 under non-conservative transverse force is investigated, see Fig. 10.13. Three beams are used for this problem. One vertical beam of length $L_1 = 120$ and two

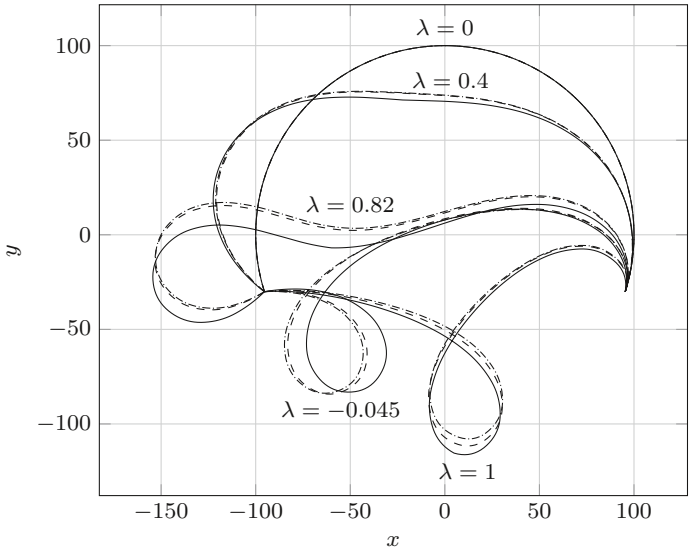

Fig. 10.11 Deformed configurations of the different beam models for load parameters $\lambda \in \{0, 0.4, 0.82, -0.045, 1\}$. The Timoshenko beam model is depicted by solid lines, the Euler–Bernoulli beam by dashed lines and the inextensible Euler–Bernoulli beam model by dashdotted lines.

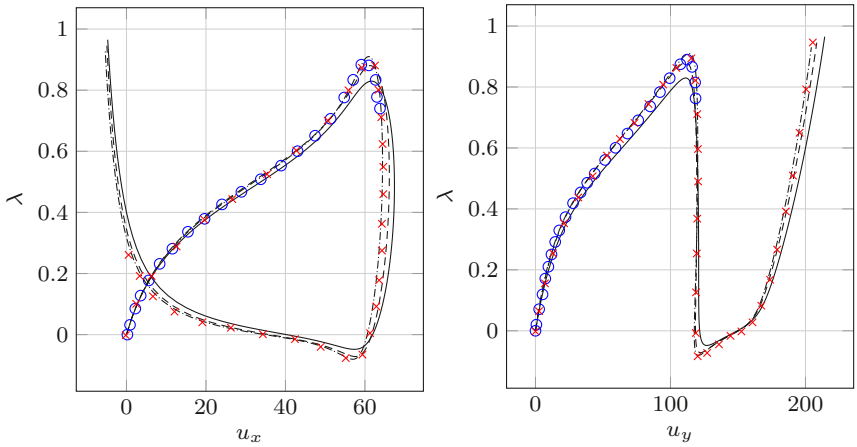

Fig. 10.12 Load deflection curves for the horizontal displacement $u_x = x(L_1)$ and vertical displacement $u_y = -(y(L_1) - 100)$ of the point of applied load. The Timoshenko beam model is depicted by solid lines, the Euler–Bernoulli beam by dashed lines and the inextensible Euler–Bernoulli beam model by dashdotted lines. The results of Dadeppo and Schmidt (1975) are depicted by blue circles, the ones computed by Simo and Vu-Quoc (1986) by red crosses.

horizontal ones, the first of length $L_2 = \frac{1}{5}L_1$, the second one of length $L_3 = \frac{4}{5}L_1$. The three beams are connected using bilateral constraints for the corresponding positions and angles. At the point where the two horizontal beams meet, a non-conservative load $P = \lambda 40 \cdot 10^3$ is applied under the angle $\pi/2$. The three beams are build with Young's modulus $E = 7.2 \cdot 10^6$, shear modulus $G = E/(2 + 2\nu)$, Poisson's ratio $\nu = 0.3$, cross section area $A = 6$, moment of inertia $I_3 = 2$, axial stiffness $E_1 = EA$, shear stiffness $E_2 = GA$ and flexural stiffness $F_3 = EI_3$.

The vertical beam was discretized using $n = 20$ quadratic B-spline elements ($p = 2$, $p_{\sigma_1} = 1$), the small and large horizontal parts were discretized with 4 and 16 quadratic B-spline elements, respectively. The numerical solutions were obtained using the previously presented linear arc length solver with $\Delta s = 600$ and a convergence tolerance of 10^{-6} with respect to the maximum absolute error of the extended residual (10.73).

Fig. 10.13 shows five representative configurations of the different beam models. Only for the force increments $\lambda = 0.885$ and $\lambda = -0.345$ minor differences between the Timoshenko beam model and the two Euler–Bernoulli beams can be noted. This is due to the large axial and shear stiffness parameters introduced by Argyris and Symeonidis (1981), which where taken for comparative purposes.

In Fig. 10.14, the load deflection curves for the horizontal and vertical deflections are depicted. The computed results are in good accordance with the ones reported by (Argyris and Symeonidis, 1981) and (Simo and Vu-Quoc, 1986), both of which present Timoshenko beam models. In the magnified areas small differences between the Timoshenko beam and the two Euler–Bernoulli beams can be recognized. The configurations for both Euler–Bernoulli beam models cannot be distinguished.

10.6.6 Natural Frequencies of a Two Sided Pinned Euler–Bernoulli Beam

In this example the natural frequencies of a two sided pinned beam of length $L = 2\pi$, axial stiffness $E_1 = 0.1$, flexural stiffness $F_3 = 1$ and mass density $\rho_0 = 1$ are compared with the ones computed using the Euler–Bernoulli beam finite element model. For the numerical computation different polynomial degrees $p \in \{2, 3, 5\}$ and element numbers $n \in \{32, 128, 512\}$ were compared and their influence on the accuracy was investigated.

The analytic solutions for the eigenvalues are well known in literature, e.g., Graff (1975). They can be derived from the governing equation

$$a^2 y''''(s,t) + \ddot{y}(s,t) = 0 \,, \quad a^2 = EI/\rho A \,. \tag{10.74}$$

By substituting the separation ansatz $y(s,t) = Y(s)T(t)$ into (10.74) and separating the spatial and time dependent variables we get

$$a^2 \frac{Y''''}{Y} = \frac{\ddot{T}}{T} = \omega^2 \,. \tag{10.75}$$

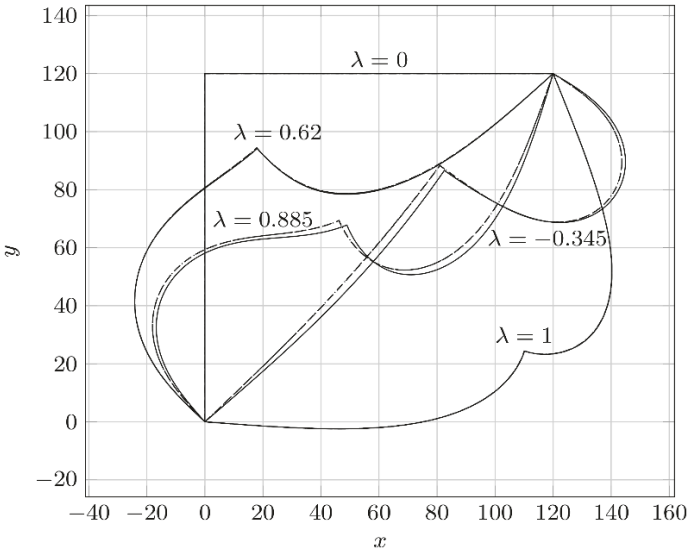

Fig. 10.13 Deformed configurations of the different beam models for load parameters $\lambda \in \{0, 0.62, 0.885, -0.345, 1\}$. The Timoshenko beam model is depicted by solid lines, the Euler–Bernoulli beam by dashed lines and the inextensible Euler–Bernoulli beam model by dashdotted lines.

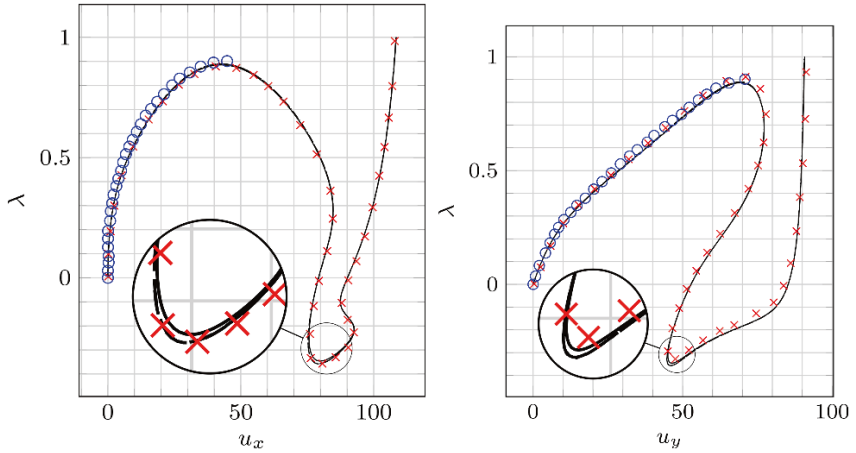

Fig. 10.14 Load deflection curves of the point of applied force for the horizontal displacement $u_x = x(L_2) - 120$ and the vertical displacement $u_y = -(y(L_2) - 120)$. The Timoshenko beam model is depicted by solid lines, the Euler–Bernoulli beam by dashed lines and the inextensible Euler–Bernoulli beam model by dashdotted lines. The results of Argyris and Symeonidis (1981) are depicted by blue circles, the ones reported by Simo and Vu-Quoc (1986) using red crosses.

The solution of the left hand side, a fourth order ordinary differential equation, is given by

$$Y(s) = C_1 \sin(\beta s) + C_2 \cos(\beta s) + C_3 \sinh(\beta s) + C_4 \cosh(\beta s) \ , \ \beta^4 = \frac{\omega^2}{a^2} \ . \tag{10.76}$$

The second order ordinary differential equation of the right hand side is fulfilled by

$$T(t) = A \cos(\omega t) + B \sin(\omega t) \ . \tag{10.77}$$

For a two sided pinned beam, the boundary conditions in terms of $Y(s)$, are given by $Y(0) = Y''(0) = Y(L) = Y''(L) = 0$. Inserting these boundary conditions into (10.76), the constants $C_2 = C_3 = C_4 = 0$ can be identified. Thus, the frequency equation

$$\sin(\beta L) = 0 \ , \quad \beta L = n\pi \ , \quad n = 1, 2, \dots \tag{10.78}$$

is obtained. The radial and cyclical frequencies for the two sided pinned beam are given by

$$\omega_n = a \left(\frac{n\pi}{L} \right)^2 \ , \quad f_n = \frac{a\pi n^2}{2L^2} \ , \quad n = 1, 2, \dots \ . \tag{10.79}$$

The corresponding normal modes read

$$Y_n(s) = \sin(\beta_n s) \ , \quad \beta_n = \frac{n\pi}{L} \ , \quad n = 1, 2, \dots \ . \tag{10.80}$$

The numerical eigenfrequencies were computed using the linearized equilibrium equation

$$\mathbf{M}\ddot{\mathbf{q}} - \mathbf{K}\mathbf{q} = \mathbf{0} \ , \tag{10.81}$$

with stiffness matrix in (10.52). For the mass matrix (10.50), the term involving I_3 was omitted. This is in accordance with the linearized partial differential equation (10.74), where rotatory effects of the cross sections are not included. Substituting the solution ansatz $\mathbf{q} = \boldsymbol{\phi} e^{\lambda t}$, $\ddot{\mathbf{q}} = \lambda^2 \boldsymbol{\phi} e^{\lambda t}$, the corresponding eigenvalue problem is obtained by multiplying $e^{-\lambda t}$ from the right and using $\lambda = i\omega$

$$\left(-\mathbf{K} - \omega^2 \mathbf{M} \right) \boldsymbol{\phi} = \mathbf{0} \ . \tag{10.82}$$

This can be solved numerically for the normal values ω_n and their corresponding normal modes $\boldsymbol{\phi}_n$.

In Fig. 10.15 the absolute errors of the first 21 numerically computed natural frequencies with respect to the analytical ones are depicted using a semi-logarithmic axis. It can be observed that both refinement strategies lead to better agreements of the finite element approximation with the analytical normal frequencies. For the reported normal frequencies, the influence of the polynomial degree elevation of the chosen B-spline shape functions is larger than increasing the number of elements. For the finest refinement level ($p = 5$, $n = 512$) all shown normal frequencies are computed up to machine precision.

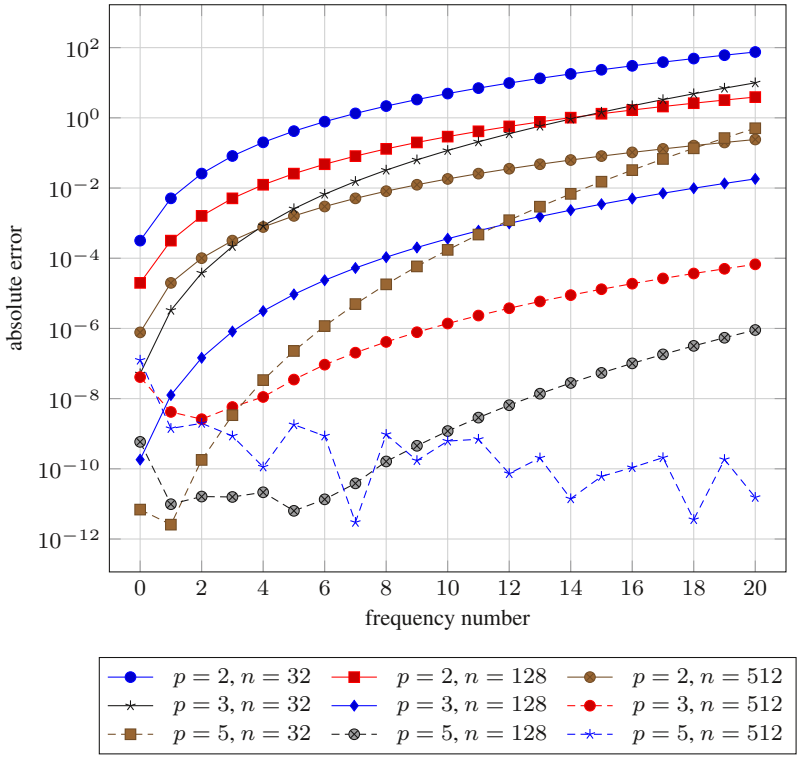

Fig. 10.15 Error in the first 21 natural frequencies of the finite element implementation of the Euler–Bernoulli beam model.

10.7 Conclusion

Starting from a variational framework, this article presents a finite element analysis of planar nonlinear classical beam theories. For discretizing the total virtual work, B-splines are chosen for both ansatz and test functions. This led to three kinematically different beam finite element models, either by finding a minimal set of kinematical descriptors, or by imposing additional constraint equations. All different beam models were studied in a variety of numerical experiments. Reproduction of analytical solutions and numerical results reported in classical beam finite element literature show the power and versatility of the presented numerical implementations.

Thus, the investigated discretization approach is well-suited for application to large systems of beams, e.g., pantographic structures (Andreaus et al, 2018; dell'Isola et al, 2018, 2019). Due to the lack of ready-to-use beam finite element models (dell'Isola et al, 2016), or because of their simple but performant implementation (Turco et al, 2016; Giorgio, 2020), discrete Hencky-type beam models are often used in literature.

Further research should include a finite element discretization approach for spatial beam models. This leads to a variety of applications, including out of plane deformation of the above-mentioned pantographic structures and their buckling and post-buckling behavior (Giorgio et al, 2017).

Acknowledgements This research has been funded by the Deutsche Forschungsgemeinschaft (DFG, German Research Foundation) under Grant No. 405032572 as part of the priority program 2100 Soft Material Robotic Systems.

References

Andreaus U, Spagnuolo M, Lekszycki T, Eugster SR (2018) A Ritz approach for the static analysis of planar pantographic structures modeled with nonlinear Euler-Bernoulli beams. Continuum Mechanics and Thermodynamics 30(5):1103–1123

Argyris JH, Symeonidis S (1981) Nonlinear finite element analysis of elastic systems under non-conservative loading-natural formulation. part I. quasistatic problems. Computer Methods in Applied Mechanics and Engineering 26(1):75 – 123

Arnold M, Brüls O (2007) Convergence of the generalized-α scheme for constrained mechanical systems. Multibody System Dynamics 18(2):185–202

Bisshopp KE, Drucker DC (1945) Large deflection of cantilever beams. Quart Appl Math 3 (1945), 272-275

de Boor C (1972) On calculating with B-splines. Journal of Approximation Theory 6(1):50 – 62

de Boor C (1978) A Practical Guide to Splines. Applied Mathematical Sciences, Springer New York

Brüls O, Acary V, Cardona A (2014) Simultaneous enforcement of constraints at position and velocity levels in the nonsmooth generalized-α scheme. Computer Methods in Applied Mechanics and Engineering 281:131–161

Brüls O, Acary V, Cardona A (2018) On the constraints formulation in the nonsmooth generalized-α method. In: Advanced Topics in Nonsmooth Dynamics, Springer, pp 335–374

Byrd PF, Friedman MD (1954) Handbook of Elliptic Integrals for Engineers and Physicists. Die Grundlehren der mathematischen Wissenschaften, Springer

Cazzani A, Malagù M, Turco E (2016a) Isogeometric analysis of plane-curved beams. Mathematics and Mechanics of Solids 21(5):562–577

Cazzani A, Malagù M, Turco E, Stochino F (2016b) Constitutive models for strongly curved beams in the frame of isogeometric analysis. Mathematics and Mechanics of Solids 21(2):182–209

Cottrell JA, Hughes TJR, Bazilevskij JJ (2009) Isogeometric analysis: toward integration of CAD and FEA. Wiley, Chichester

Cox MG (1972) The numerical evaluation of B-splines. IMA Journal of Applied Mathematics 10(2):134–149

Crisfield MA (1981) A fast incremental/iterative solution procedure that handles "snap-through". Computers & Structures 13(1):55 – 62

Crisfield MA (1991) Non-linear Finite Element Analysis of Solids and Structures: Essentials. Non-Linear Finite Element Analysis of Solids and Structures, Wiley

Dadeppo DA, Schmidt R (1975) Instability of Clamped-Hinged Circular Arches Subjected to a Point Load. Journal of Applied Mechanics 42:894

dell'Isola F, Giorgio I, Pawlikowski M, Rizzi N (2016) Large deformations of planar extensible beams and pantographic lattices: Heuristic homogenisation, experimental and numerical examples of equilibrium. Proceedings of The Royal Society A 472

dell'Isola F, Seppecher P, et al (2018) Pantographic metamaterials: an example of mathematically driven design and of its technological challenges. Continuum Mechanics and Thermodynamics pp 1–34

dell'Isola F, Seppecher P, et al (2019) Advances in pantographic structures: Design, manufacturing, models, experiments and image analyses. Continuum Mechanics and Thermodynamics 31:1231–1282

Eugster SR, Harsch J (2020) A variational formulation of classical nonlinear beam theories. In: Abali BE, Giorgio I (eds) Developments and Novel Approaches in Nonlinear Solid Body Mechanics, Advanced Structured Materials, Springer

Farin GE (1997) Curves and Surfaces for Computer-aided Geometric Design: A Practical Guide. No. Bd. 1 in Computer science and scientific computing, Academic Press

Giorgio I (2020) A discrete formulation of Kirchhoff rods in large-motion dynamics. Mathematics and Mechanics of Solids 25(5):1081–1100

Giorgio I, Rizzi N, Turco E (2017) Continuum modelling of pantographic sheets for out-of-plane bifurcation and vibrational analysis. Proceedings of the Royal Society A: Mathematical, Physical and Engineering Science 473:20170,636

Gontier C, Vollmer C (1995) A large displacement analysis of a beam using a CAD geometric definition. Computers & Structures 57(6):981 – 989

Graff KF (1975) Wave motion in elastic solids. Clarendon Press, Oxford

Greco L, Cuomo M (2013) B-spline interpolation of Kirchhoff-Love space rods. Computer Methods in Applied Mechanics and Engineering 256(0):251–269

Greco L, Cuomo M (2014) An implicit G^1 multi patch B-spline interpolation for Kirchhoff–Love space rod. Computer Methods in Applied Mechanics and Engineering 269:173 – 197

Hairer E, Wanner G (2002) Solving Ordinary Differential Equations II, 2nd edn. Springer

Hughes T, Cottrell J, Bazilevs Y (2005) Isogeometric analysis: CAD, finite elements, NURBS, exact geometry and mesh refinement. Computer Methods in Applied Mechanics and Engineering 194(39):4135 – 4195

Jay OL, Negrut D (2009) A Second Order Extension of the Generalized–α Method for Constrained Systems in Mechanics, Springer, pp 143–158

Leine R, van de Wouw N (2007) Stability and Convergence of Mechanical Systems with Unilateral Constraints. Lecture Notes in Applied and Computational Mechanics, Springer

Lunk C, Simeon B (2006) Solving constrained mechanical systems by the family of newmark and α-methods. Zeitschrift für Angewandte Mathematik und Mechanik 86(10):772–784

Piegl LA, Tiller W (1997) The NURBS Book, 2nd edn. Springer

Quarteroni A, Sacco R, Saleri F (2000) Numerical Mathematics. Texts in applied mathematics, Springer

Riks E (1979) An incremental approach to the solution of snapping and buckling problems. International Journal of Solids and Structures 15(7):529 – 551

Rohatgi A (2019) Webplotdigitizer. https://automeris.io/WebPlotDigitizer

Schöneberg IJ (1946) Contributions to the problem of approximation of equidistant data by analytic functions: Part a.–on the problem of smoothing or graduation. A first class of analytic approximation formulae. Quarterly of Applied Mathematics 4(1):45–99

Simo JC, Vu-Quoc L (1986) A three-dimensional finite-strain rod model. part II: Computational aspects. Computer Methods in Applied Mechanics and Engineering 58:79–116

Stoer J, Bartels R, Gautschi W, Bulirsch R, Witzgall C (2002) Introduction to Numerical Analysis. Texts in Applied Mathematics, Springer New York

Turco E, dell'Isola F, Cazzani A, Rizzi NL (2016) Hencky-type discrete model for pantographic structures: numerical comparison with second gradient continuum models. Zeitschrift für angewandte Mathematik und Physik 67(4):85